

Predicting the Failure of Aluminum Exposed to Simulated Fire and Mechanical Loading Using
Finite Element Modeling

Katherine Marie Arthur

Thesis submitted to the faculty of the Virginia Polytechnic Institute and State University in
partial fulfillment of the requirements for the degree of

Master of Science
In
Engineering Mechanics

Scott W. Case
Brian Y. Lattimer
Norman E. Dowling

May 12, 2011
Blacksburg, VA

Keywords: (Fire, Compression Loading, Simulation, Finite Element Method)

Predicting the Failure of Aluminum Exposed to Simulated Fire and Mechanical Loading Using Finite Element Modeling

Katherine Marie Arthur

Abstract

The interest in the use of aluminum as a structural material in marine applications has increased greatly in recent years. This increase is primarily due to the low weight of aluminum compared to other structural materials as well as its ability to resist corrosion. However, a critical issue in the use of any structural material for naval applications is its response to fire.

Past experience has shown that finite element programs can produce accurate predictions of failure of structural components. Parameter studies conducted within finite element programs are often easier to implement than corresponding studies conducted experimentally.

In this work, the compression-controlled failures of aluminum plates subjected to an applied mechanical load and an applied heat flux (to simulate fire) were predicted through the use of finite element analysis. Numerous studies were completed on these finite element models. Thicknesses of the plates were varied as well as the applied heat flux and the applied compressive stresses. The effect of surface emissivity along with the effect of insulation on the exposed surface of the plate was also studied. The influence of the initial imperfection of the plates was also studied. Not only were the physical conditions of the model varied but the element type of both the solid and shell models as well as the mesh density were also varied. Two different creep laws were used to curve fit raw creep data to understand the effects of creep in the buckling failure of the aluminum plates.

These predictions were compared with experiments (from a previous study) conducted on aluminum plates of approximately 800mm in length, 200mm in width, 6-9mm in thickness and clamped at both ends to create fixed boundary conditions. A hydraulic system and a heater were used to apply the compressive load and the heat flux respectively. Comparisons between predicted and experimental results reveal that finite element analysis can accurately predict the compression-controlled failure of aluminum plates subjected to simulated fire. However, under certain combinations of the applied heat flux and compressive stress, the mesh density as well as the choice of element may have a significant impact on the results. Also, it is undetermined which creep curve-fitting model produces the most accurate results due to the influence of other parameters such as the initial imperfection.

Dedication

I would like to dedicate this thesis to my family, especially my mother and father. Their love and support has given me the self confidence I need to be successful. I appreciate all of their hard work in helping me achieve my goals. I also would like to thank my close friends who have given me support throughout this entire process. Also, a special thanks goes to Ryan and his family for all of their care and support and never allowing me to fall behind.

Acknowledgements

First, I would like to thank Dr. Case for allowing me the opportunity to work with him on such a wonderful and challenging project the past two years. Dr. Case consistently made himself available for any questions or concerns I had about the project. His support and guidance has allowed me to present something that I can be proud of. I greatly appreciate all of Dr. Case's time and effort that he put into helping me to meet deadlines and achieve the goals of this project.

Dr. Lattimer has also been a great influence in this project. Our weekly meetings along with Dr. Case allowed deadlines and goals to be met. Dr. Lattimer also made himself available outside of those meetings with any questions I had. I greatly appreciate all of Dr. Lattimer's support throughout the past two years.

Dr. Dowling taught a course in Mechanics of Materials which I attended in the Spring of 2010. This course allowed me to realize Dr. Dowling's expertise in materials would be a great asset to this project. I greatly appreciate the discussions we have had about my project as well as the help he has given me in preparing my thesis.

Stefanie Feih and Everson Kandare both have been incredible resources throughout this project. Their knowledge of finite element analysis and materials has given me the ability to draw in depth conclusions and extend my knowledge on the subjects. I would also like to extend a special thanks to Stefanie for readily making herself available for any questions I had about the project.

I would also like to thank Emily Fogle, Ryan Matulich, and Patrick Summers for all of their contributions to this project as well as their support in my work.

Table of Contents

Dedication	iii
Acknowledgements	iii
List of Figures	vi
List of Tables	ix
1. Literature Review	1
1.1 Historical use of aluminum as a structural material in shipbuilding	1
1.2 Constitutive properties and mechanical behavior of aluminum alloys	3
1.3 General behavior of aluminum structures exposed to elevated temperatures	10
1.4 Previous experimental work and finite element simulations of the buckling failure of aluminum plates exposed to elevated temperature	17
1.5 Previous work using strength reduction (knock-down) factors to model welded aluminum material in finite element simulations	22
1.6 Discussion	25
2. Validation of intermediate scale buckling tests of one-sided heating of 5083-H116 aluminum plates	26
2.1 Introduction	26
2.2 Experimental Characterization	26
2.3 Building the Finite Element Model	28
2.3.1 General Description of the Model	28
2.3.2 Description of Abaqus Shell and Solid Elements	28
2.3.3 Mesh Discretization	31
2.4 Physical Boundary Conditions	32
2.5 Constitutive Properties	33
2.5.1 Stress Strain Information	33
2.5.2 Creep Fitting Laws	34
2.6 Thermal Boundary Conditions	38
2.7 Initial Imperfections	40
2.8 Results	42
2.8.1 Results Prior to Mesh Convergence Study	42
2.8.2 Mesh Convergence Study	46

2.8.2.1	Convergence of Buckling Results	47
2.8.2.2	Convergence of Coupled Temperature-Displacement Step	48
2.8.2.3	Effect of Shell Element Type	49
2.8.2.4	Effect of Solid Element Type	51
2.8.2.5	Comparison of Solid and Shell Element Types	54
2.9	Final Results	57
2.9.1	Shell Elements Final Results	57
2.9.1.1	Importance of Creep in Compression-Controlled Failure	57
2.9.1.2	Abaqus Power Law Creep Results	58
2.9.1.3	Dorn-Harmathy Creep Law Results	59
2.9.2	Effect of Emissivity on Plate Surface Temperature	61
2.9.3	Effect of Insulation on the Exposed Surface	63
2.10	Discussion of Results	66
3.	Conclusions & Future Work	67
	List of Resources	68

List of Figures

Figure 1. Classification of aluminum alloys	4
Figure 2. Aluminum plated structure	8
Figure 3. Creep strain vs. time curve	12
Figure 4. Extruded cross section of bridge deck	22
Figure 5. Large-Scale extent of bridge deck	22
Figure 6. Knock-down method	23
Figure 7. Intermediate scale tests experimental setup	27
Figure 8. (a) curved deformation of a quadratic element under a pure bending moment (b) shear deformation of a linear element under a pure bending moment as a result of shear locking	29
Figure 9. (a) linear solid element with poor aspect ratio (b) linear solid element with excellent aspect ratio	29
Figure 10. (a) Graphic of Mesh Discretization (b) Close-up of mesh through thickness	31
Figure 11. Close-up of elements through thickness – 8mm plate	32
Figure 12. Depiction of fixed boundary conditions on bottom portion of plate	32
Figure 13. Selected stress-strain curves for 5083-H116 aluminum	33
Figure 14. Elastic modulus vs. temperature	34
Figure 15. Yield Strength (0.2% offset) vs. temperature	34
Figure 16. Creep strain vs. time 50 MPa applied stress	35
Figure 17. Creep strain vs. time 65 MPa applied stress	35
Figure 18. Creep strain vs. time 80 MPa applied stress	35
Figure 19. Creep strain vs. time 90 MPa applied stress	35
Figure 20. Dorn-Harmathy Creep strain vs. time – various applied stresses at 350°C	36
Figure 21. Dorn-Harmathy Creep strain vs. time – various temperatures with an applied stress of 50 MPa	37
Figure 22. Heat flux gauge locations	39
Figure 23. Partitioned model in Abaqus	39
Figure 24. Normalized heat flux pattern	39
Figure 25. Flowchart of initial imperfection implementation in Abaqus	41

Figure 26. Nodal temperature vs. time at the center of the plate – 38 kW/m ² applied heat flux and 14.61 MPa applied stress	44
Figure 27. Out-of-plane deflection vs. time at center of plate – 38 kW/m ² applied heat flux and 14.61 MPa applied stress	44
Figure 28. In-plane deflection vs. time at top of plate – 38 kW/m ² applied heat flux and 14.61 MPa applied stress	45
Figure 29. Out-of-plane deflection results – 9mm aluminum plate with 38 kW/m ² applied heat flux and 5.19 MPa applied stress	46
Figure 30. Coarsest mesh – 400 elements	47
Figure 31. Final mesh – 76,800 elements	47
Figure 32. Finest mesh – 614,400 elements	47
Figure 33. Critical buckling stress vs. number of elements – C3D8 element type	48
Figure 34. Out-of-plane deflection vs. time curve for C3D8T element type – 19 kW/m ² heat flux and 14.9 MPa applied stress	48
Figure 35. Out-of-plane deflection vs. time curve for S4T element type – 19 kW/m ² heat flux and 14.9 MPa applied stress	49
Figure 36. Out-of-plane deflection vs. time curve for S4T element type – 8 kW/m ² heat flux and 19.43 MPa applied stress	50
Figure 37. Out-of-plane deflection vs. time curve – comparison between shell element types (S4T, S8RT, and SC8RT)	51
Figure 38. Out-of-plane deflection vs. time curve – comparison between C3D8T and C3D20T Elements	51
Figure 39. Out-of-plane deflection vs. time curve – comparison between reduced integration hourglass controls	53
Figure 40. Artificial Strain Energy (kJ) vs. time (s) curve	53
Figure 41. Out-of-Plane Deflection vs. Time Curve – 8mm thick plate with an applied heat flux of 8 kW/m ² and applied stress of 19.43 MPa	54
Figure 42. Out-of-Plane Deflection vs. Time Curve – 6mm thick plate with an applied heat flux of 38 kW/m ² and applied stress of 4.05 MPa	55
Figure 43. Out-of-Plane Deflection vs. Time Curve – 8mm thick plate with an applied heat flux of 38 kW/m ² and applied stress of 3.39 MPa	55

Figure 44. Out-of-Plane Deflection vs. Time Curve – 6mm thick plate with an applied heat flux of 8 kW/m ² and applied stress of 14.61 MPa	56
Figure 45. Out-of-Plane Deflection vs. Time – applied stress of 7.19 MPa and applied heat flux of 38 kW/m ²	57
Figure 46. Experimental vs. Predicted Times to Failure – S4T elements with Abaqus power law creep model	58
Figure 47. Experimental vs. Predicted Times to Failure – S4T elements with the Dorn-Harmathy creep law	59
Figure 48. Predicted times to failure for the Abaqus power law creep vs. the Dorn-Harmathy creep law models – S4T elements	60
Figure 49. Creep Strain vs. Time - 50°C 4MPa applied stress	60
Figure 50. Creep Strain vs. Time - 300°C 10MPa applied stress	60
Figure 51. Effect of Emissivity on exposed and unexposed surfaces – Nodal Temperature vs. Time – 19 kW/m ² applied heat flux	62
Figure 52. Nodal Temperature vs. Time with insulation on the exposed surface – 38 kW/m ² applied heat flux.....	63
Figure 53. Out-of-Plane Deflection vs. Time with insulation on the exposed surface – 38 kW/m ² applied heat flux and 16.3 MPa applied stress	64
Figure 54. In-Plane Deflection vs. Time with insulation on the exposed surface – 38 kW/m ² applied heat flux and 16.3 MPa applied stress	65

List of Tables

Table 1. Mesh discretization prior to mesh convergence study	31
Table 2. Mesh discretization following the mesh convergence study	32
Table 3. Material constants for Abaqus creep power law	35
Table 4. Dorn-Harmathy Creep Law Material Constants	36
Table 5. Moment of Inertia, cross-sectional area, critical buckling stress values	42
Table 6. Numerical buckling stresses prior to the mesh convergence study	43
Table 7. Numerical buckling stresses following the mesh convergence study	43

Chapter 1 – Literature Review

1.1 - Historical use of aluminum as a structural material in shipbuilding

Aluminum was first discovered in 1808 by Sir Humphry Davy who termed it “aluminum.” It then wasn’t until 1886 when the Hall-Heroult electrolytic process was invented that aluminum became commercially available. Over one-hundred years ago, nearing the 19th century, papers concerning new uses of aluminum as a shipbuilding material were presented in front of The Society of Naval Architects and Marine Engineers [1].

According to Muckle [2], the first appearance of aluminum in shipbuilding was about one-hundred years ago. A small torpedo ship was created using aluminum as the main structural component in the hull portion of the ship. The use of aluminum in the hull made this torpedo boat weigh about two and half tons less than what it would with a different structural material, such as steel. Sielski [1] and Muckle [2] both point out that around 1895 the *Defender* became one among many well known small vessels that utilized aluminum as a structural material.

During the period of time after the turn of the century to about 1929 there were very few papers concerned with the use of aluminum in shipbuilding. Around this time, though, interest grew in understanding how to incorporate two different materials (different elastic modulus, yield strength, ultimate tensile strength, thermal expansion, etc.) into a ship design. Because of the advances made in the analysis of steel reinforcement in concrete, this was not a new challenge [2].

In the 1930s and 1940s interest in using aluminum in larger vessels grew mainly due to its corrosion resistance and lightweight. Even though this interest grew aluminum was still mainly used in small vessels. The *Diana 11*, a smaller ship, achieved many long successful years at sea with aluminum as its main construction material [2]. During this time, aluminum was used in larger vessels only in structures that were not part of the main load bearing structure of the ship. For example, in 1939, a large vessel named the S.S. *Fernplant* used aluminum for the deckhouse structure of the ship. (The deckhouse did not carry significant loads [2]). These deckhouse structures made of aluminum were also used on U.S. Navy combatant ships [3]. The U.S. Navy utilized aluminum for this type of structure for over 70 years.

During the decades following these new applications of aluminum, more and more engineers and shipbuilders became proponents of using aluminum in the superstructure of large vessels [1]. Aluminum’s use as a main load-carrying structural material on large ships was not heavily discussed until about the 1960s. Muckle [2] was one of many who investigated the use of aluminum as main structural members in large vessels. During these investigations it was found that using aluminum instead of other materials such as steel would relieve about 50-55% of the structural weight. Further investigations into the use of aluminum in cargo type ships revealed that aluminum also had excellent corrosion resistance [2]. As a result, experimental testing of the corrosion resistance of aluminum began in 1944 and validated such claims [1].

Later in the 1960s, investigations revealed another application of aluminum: large vessel carriers of liquid methane. This application was chosen because aluminum has superior

properties to steel at low temperatures. Steel has the tendency to behave as a brittle material at low temperatures when aluminum does not [2]. Muckle [2] states that the one problem standing in the way of greater adaptation of aluminum is the cost. The cost of shipbuilding steel in the 1960s was much less than the cost of aluminum.

Over the subsequent decades, ships became larger and more intricate in design. This increased complexity sparked more interest in using aluminum in larger vessels due to its low weight to density ratio. However, in the 1980s the U.S. Navy began to question the use of aluminum in their combatant ships. Questions of the material's ability to withstand onboard fires as well as maintenance problems led to the ban of certain aluminum alloys for major U.S. Navy combatant ships. It was not until the 1990's that aluminum was used for the hulls of high-speed merchant vessels [3]. Sielski and Taylor [3] state that many of these types of high-speed ships were faster than Navy combatant ships. Soon after, the U.S. Navy began to model their combatant ships after these high-speed vessels.

Since the turn of the 20th century, interest in aluminum increased exponentially. There are still many unanswered questions surrounding the use of aluminum in structural applications. One of the main questions surrounding aluminum is whether it can withstand elevated temperature situations where fire is a concern. Because of its low melting temperature the use of aluminum structures in possible fire scenarios needs to be fully considered in its design and implementation.

1.2 - Constitutive properties and mechanical behavior of aluminum alloys

1.2.1 Advantages/disadvantages of using aluminum as a structural material

There are many advantages to using aluminum as a structural material. Among them is its low dead weight as compared to other structural materials such as steel. For example, when aluminum is used as a bridge deck material the substructure of the bridge is unaffected and does not need to be modified. Another advantage of aluminum is its good corrosion resistance as compared to steel and its durability as compared to timber. This can reduce material expenses and could be considered environmentally friendly [4].

Corrosion of metals used in structures can be a significant problem. Two examples of specific types of corrosion that are apparent in aluminum structures are termed general corrosion/pitting and exfoliation. The first of these, general corrosion, causes an oxide layer to form over the surface of the aluminum material. This type of corrosion is advantageous because it can prevent more corrosion from occurring. However, if the layer does not form well over the surface of the alloy, pitting can occur. Pitting is the formation of small holes along the surface. Another type of corrosion is called exfoliation where corrosion occurs along the alloy's grain boundaries and causes the material to flake off. This occurs mainly in 5xxx series aluminum alloys that have large (over 3%) amounts of magnesium. In order to compensate for this problem the temper H116 was created to resist exfoliation [1].

There are a few disadvantages to using aluminum as a structural material. Aluminum has a low ratio of stiffness to strength as compared to other materials such as steel. Also, most aluminum sections are made to be slender. Because of this, aluminum structures are susceptible to local and global buckling. The fatigue of aluminum sections also becomes an issue as a result of the high ratio of live load to dead weight [4].

1.2.2 Classification of aluminum alloys

The mechanical properties of aluminum are entirely dependent upon the choice of alloy. Different industries such as bridge building, ship building, and the aerospace industry use very specific aluminum alloys. These industries utilize these alloys for a specific use and thus have requirements concerning the alloy's material properties such as yield strength, ultimate strength, hardness, and elastic modulus.

There are six different main aluminum alloy series: the 1xxx, 2xxx, 3xxx, 5xxx, 6xxx, and 7xxx series [5]. The two most commonly used alloys in the ship building industry are the 5xxx and 6xxx series. The 5xxx series aluminum alloy have magnesium as the main component while the 6xxx series has both magnesium and silicon as the main components. These components form precipitates of magnesium silicide which allows the alloy to be heat-treated. The two most common alloys used in the aerospace industry are the 2xxx and 7xxx series [1]. Specifically, the series presented above (2xxx through 7xxx series) are separated by the main element present in the alloy. For example, the main elements in the 2xxx and 7xxx series are Copper and Zinc respectively. Also, for the 5xxx and 6xxx series the main element present is Magnesium and Magnesium/Silicon respectively. The second number in the series designation

signifies any modifications done to the alloy and the other two numbers are used to separate specific alloys in that same series from one another [6].

In general, there are four different temper designations associated with aluminum alloys: F (As-Fabricated), O (Annealed), H (Strain-Hardened), and T (Solution Heat-Treated). These are symbolized with a capital letter subsequent to the series number. Located next to the capital letter temper designation is a number which signifies several different types of processes associated with that specific temper. For example, H1 signifies a temper which is strain-hardened only, as opposed to H2 which signifies a temper which is both strain-hardened and partially annealed. Additionally, another number is attached to the temper designation. This signifies the minimum ultimate tensile strength for the specific degree of strain-hardening. A third number may also be used to represent variations associated within the two digit temper designation [6].

Specifically, there are about four processes associated with temper designation H (strain-hardened) and about ten processes associated with temper designation T (solution heat-treated). The processes in the H temper either utilize strain-hardening only or utilize strain-hardening and something else in addition, such as partial annealing, or cold working. The processes involved in the T temper involve heat treatment processes, cooling processes, cold working, shaping processes, as well as naturally aging [6].

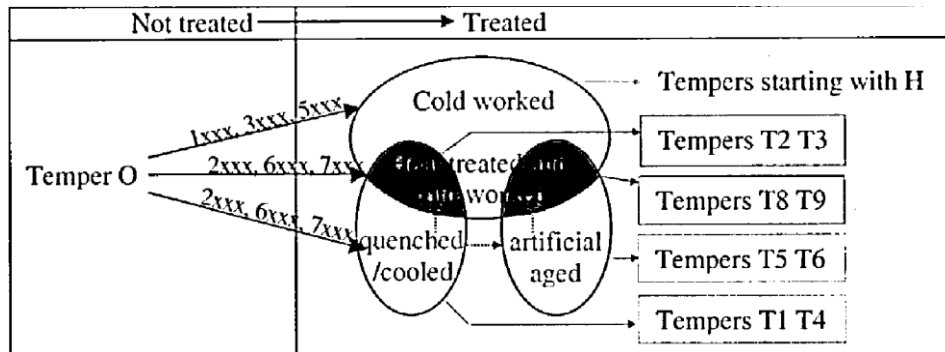


Figure 1. Classification of aluminum alloys – Reproduced from [5] with permission of F. Soetens, 2011.

Each of the aluminum alloy series utilizes a specific temper designation. The 1xxx, 3xxx, and 5xxx series can only utilize the temperature designation H, while the 2xxx, 6xxx, and 7xxx series alloys can utilize various T temper designations. Figure 1 from [5] depicts the different types of tempers associated with each of the aluminum series starting from their annealed temper O. The aerospace industry, as stated above, uses mainly 2xxx and 7xxx series aluminum alloys which can only use the process of solution heat-treatment (whether that be cold working, or heat-treated, or naturally aged). The 5xxx and 6xxx series of aluminum alloys are mainly used in the ship industry and have the H and T temper designation respectively. These series have excellent corrosion resistance which is vital on a ship.

Mrowka-Nowotnik et al. [7] ran a series of experimental tests which investigated the effect of treatment processes on the microstructure of 6xxx series aluminum alloys. The additional elements found in 6xxx series aluminum alloys are mainly those of magnesium and

silicon. Iron and magnesium are always present in aluminum alloys. Even small traces of these transition metals can cause new phase components in the alloy to form. Numerous other phases associated with iron can also be formed: Al-Fe-Si, Al-Fe, and Al-Fe-Mn-Si. These different phases cause the alloy to exhibit different physical and mechanical properties based on phases present in the material [7]. They also carried out an investigation on two 6xxx series aluminum alloys: 6005 and 6082. The investigation examined how different cooling modes affected the alloys at a micro and macro scale. They also investigated how different heating temperatures affected the aluminum alloys. Each of the 6xxx series samples was initially heated in an induction furnace to a temperature of about 570°C for about four to six hours and then were cooled using four different cooling modes: water and oil quench, or air and slow furnace cooling. After the specimens cooled they were subjected to heat treatment with a variance in heat treatment temperature from about 510 to 580°C. Finally, the specimens were aged naturally at room temperature for 120 hours [7].

Mrowka-Nowotnik et al. reveal a graphic of the microstructure of the aluminum alloys samples in their as-cast state. Precipitates of the intermetallic phases were found mainly around the cell boundaries and were formed during the casting process. During the hot extrusion forging process, the precipitates of the intermetallic phases tended to arrange themselves in the direction of plastic deformation. This forms a band like structure in the direction of the plastic flow. Larger particles may reduce their size due to this arrangement. Different cooling treatments caused the hardness value to change. Mrowka-Nowotnik et al. found that the highest value was found from cooling the specimens in water and the lowest hardness value was found from slow cooling the specimens in the furnace. They also observed that after natural aging the specimens showed another increase in hardness level. The hardness increases most during the initial phases of aging; during the first three hours. After about twenty hours, the hardness value peaked. Finally, the hardness of the aluminum alloy 6005 was unaffected by the solution temperature because the amount of hardening particles formed during the aging process was much less than that of the aluminum alloy 6082.

1.2.3 Typical welding processes for aluminum alloys

The two most common welding processes used on aluminum alloys are metal inert gas (MIG) or tungsten inert gas (TIG) welding. However, in 1991, the Welding Institute in Cambridge, UK developed a welding process called friction stir welding (FSW). Users of this process range from the aerospace industry, the ship building industry and the car production industry. Initial tests on 5xxx series aluminum alloys show that the welded joints only lose about 5% of their efficiency with an insignificant impact on hardness values. Specifically, a steel welding tool with a profiled core tip is used to create frictional type heating to plastically deform the aluminum in its solid state [8]. Previous work using friction stir welding on heat-treatable aluminum alloys shows a large negative impact. This is due to the fact that the hardening precipitates in heat-treatable alloys which increase the strength of the alloys are highly affected by this welding process [9].

Liu et al [8] specifically conducted experiments to investigate how the FSW process affected 5083-H116 aluminum alloy. Utilizing the friction stir welding tool, single welding runs were made on two AA 5083-H116 plates abutted together. Samples were cut from the joint to

test the hardness values and thus the strength of the welded material. Tensile tests were performed on the joint samples of the butt-welded AA 5083-H116 plates. The results indicated that the ultimate tensile strength of the welded material was about 5-9% less than the ultimate tensile strength of the unwelded or parent material. The values for the ultimate tensile strength of the welded material was about 297.5 – 311.8 MPa while the value for the ultimate tensile strength of the unwelded material was about 323.5 MPa. The significance of FSW is twofold; it retains joint strength to almost that of the parent unwelded material and it could also be used to repair cracked welds or welds that are in need surface repairs.

Lakshminarayanan et al. [9] investigated the effects of three different welding processes on the material properties of aluminum alloy 6060. Gas tungsten arc welding (GTAW) which is related to TIG welding, metal arc welding (GMAW), which is related to MIG welding, and FSW were the three welding processes investigated in this study. MIG (GMAW) and TIG (GTAW) welding processes are used more widely than others because they are much easier to apply in practice.

Lakshminarayanan et al. found that the yield strength and the ultimate tensile strength of the unwelded or parent material were about 302 MPa and 335 MPa respectively. The GMAW welded material experiences about a 51% reduction in yield and tensile strength values. The GTAW welded material experiences about a 37% reduction in yield and tensile strength values. However, the FSW welded material only experiences about a 26% reduction in yield and tensile strength values. The hardness value in Vickers hardness of the unwelded or parent material is about 105 VHN. The GMAW welded material experiences about a 45% reduction in the hardness value while the GTAW welded material experiences about a 32% reduction in the hardness value. The FSW welded material only experiences about a 17% reduction in the hardness value. In all tests the FSW welding process produced less reduction in material properties than the GMAW and GTAW welding processes. This is due to the fact that during the friction stir welding process fine equiaxed grains and strengthening precipitates are formed.

1.2.4 The heat affected zone (HAZ)

A typical welding process such as metal inert gas welding (MIG) or tungsten inert gas welding (TIG) uses large amounts of heat to join sections of aluminum together. These welding processes cause a major reduction in strength in the heat affected zone (HAZ) – the region around the weld and the weld itself where the material structure is partially degraded as compared to the parent material [5]. Sielski and Taylor [3] state that in most aluminum design codes the strength of the HAZ is about 30-50% of the parent material strength. For some alloys this may lead to very conservative estimates of strength. More research in this area could lead to less conservative design stresses [10].

There are general “rules of thumb” as to how the width and breadth of the HAZ is measured. One rule of thumb is to assume that the heat-affected zone extends at least one inch (or 25mm) in all directions from the centerline of the weld. Another commonly used rule of thumb is to assume the HAZ extends in all directions from the centerline of the weld by a factor of three multiplied by the thickness of the welded sections. Another way to estimate the extent of

the HAZ is to take hardness measurements extending from the centerline of the weld in all directions until the hardness measurements converge to that of the parent material [10]. Paik and Duran [10] discuss the impact of different welding processes on the material properties in the heat-affected zone. Tungsten inert gas or TIG welds are generally found to have a greater affect on the softening of the welded material than metal inert gas or MIG welds. The authors state that TIG welding is not considered in this paper because it is generally not used in aluminum structural components [10].

1.2.5 Mechanical behavior of aluminum alloys

Experimental tensile test data as well as compression test data are used to describe the elastic and plastic properties of aluminum; this includes the parent and welded material. The most commonly used method to represent the stress-strain relationships of aluminum alloys is the utilization of the Ramberg-Osgood formula [10, 11],

$$\varepsilon = \frac{\sigma}{E} + 0.002 \left(\frac{\sigma}{\sigma_{0.2}} \right)^n \quad \text{Equation 1}$$

Where E is the modulus of elasticity and $\sigma_{0.2}$ is the 0.2% offset yield stress. The first term on the right hand side of Equation 1 is the elastic portion of the stress-strain relationship and the second term is the nonlinear strain hardening portion of the stress-strain curve. The value of n is determined using the yield stress value, the ultimate tensile stress and the fracture strain ($\sigma_{0.2}$, σ_T , and ε_f).

$$n = \frac{\ln 2}{\ln(1+kX)} \quad X = \frac{\sigma_T - \sigma_Y}{10\varepsilon_f} \frac{\sigma_T}{\sigma_Y} \quad \text{Equation 2}$$

k is a dimensional constant which is taken to be 0.028 mm²/N for aluminum alloys [10, 11]

Aluminum stress-strain properties particularly the yield strength, may be directly correlated with hardness measurements. The yield strength values across the width and breadth of a weld can vary tremendously depending on the type of welding process used. Utilizing this direct correlation of yield strength values across a weld profile can be estimated using Vickers hardness measurements.

In available literature most methods used to correlate Vickers hardness and yield stress involve errors up to about 25% [12]. Tekkaya [12] attributes this to the fact that when cold formed materials are in their primary stage of forming they undergo extremely large plastic strains which forces the hardening behavior to be anisotropic with non-homogeneous material properties. Tekkaya aimed to improve the accuracy of the correlation between Vickers hardness and yield stress to errors of less than 10%. He describes that during the forward extrusion process of cold formed materials there is a specific area, or the axis of the extrudate, where the plastic strain and thus the yield strength is known. Taking hardness measurements at the axis of the extruded cold formed material specimens allows for a much more accurate relationship between the strain values and hardness values.

The improved relationship between Vickers hardness (HV) and yield stress ($\sigma_{0.2}$) is found by utilizing regression curves to optimize the equivalent plastic strain that corresponds to the plastic deformation of the indentation process. Through a series of analyses Tekkaya found that the equivalent plastic strain was about 0.112. After this, he created a curve which plotted the hardness versus the yield stress found at the equivalent plastic strain. The slope of this curve is equivalent to the direct relationship of Vickers hardness to the yield strength resulting in the equation below,

$$HV = 2.475 * \sigma_{0.2} \quad \text{Equation 3}$$

There are numerous ways in which aluminum structures respond to mechanical loading. Some of these are similar to other structural materials such as steel but some are quite different and thus must be taken into consideration for design. Because of its low ratio of stiffness over strength, aluminum is extremely susceptible to buckling failures. To compensate for its susceptibilities, aluminum structures are designed to have longitudinal or transverse stiffeners which dramatically decrease the chance of large buckling failures. The buckling analyses associated with aluminum design at room temperature are very similar to those of steel design. However, there are two differences to be noted. Buckling type failures will occur much earlier in aluminum structures. This is also due to the fact that the slope of the stress-strain curve approaching the yield stress decreases more gradually than a typical steel stress-strain curve [1]. Also, as mentioned briefly, the HAZ has a large effect on the mechanical behavior of aluminum structures because of its rather significant reduction in strength.

Paik and Duran [10] studied the mechanical response, specifically the ultimate strength, of aluminum stiffened plates and panels. They also investigated the behavior of two different aluminum alloys; 5383-H116 and 5083-H116. Figure 2 below depicts a typical aluminum plate structure with longitudinal and transverse girders along with longitudinal stiffeners.

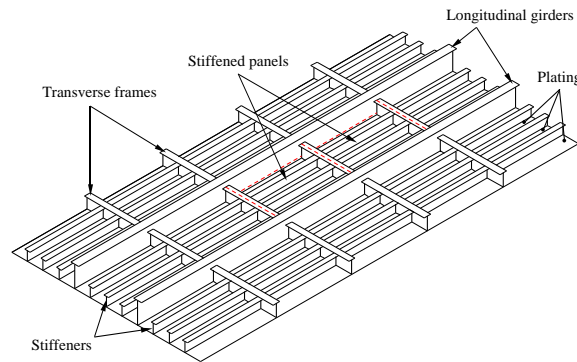


Figure 2. Aluminum plated structure – reproduced from [10] with permission of J. Paik, 2011.

Experimentally, an axial compressive load was applied to both transverse ends of an aluminum plate with simply supported boundary conditions along the entire perimeter. The stress-strain curves of both alloys produced similar results from the model until the ultimate strength was reached. After the ultimate strength was reached, the average stress of the 5083-

H116 aluminum alloy began to decline more significantly than the 5383-H116 alloy. Paik and Duran [10] conclude that this is because the yield stress reduction in the HAZ for the 5083-H116 alloy is greater than the 5383-H116 alloy. Also, due to the assumption that the HAZ extent is three times the thickness of the welded materials, the HAZ will play a larger role in thicker plates.

Paik and Duran [10] also investigated the ultimate strength of stiffened panels. Before revealing the results they first describe the possible failure modes of the aluminum stiffened panels located between the longitudinal girders and the transverse frames. These are listed below along with explanations for each:

- *General collapse of plating and stiffeners:* This occurs when the stiffeners are extremely weak and fail along with the plating as a whole. This behavior is elastic at first and then may sustain an increase in loading until the whole structure shows yielding either around the edges or in the middle of the section.
- *Collapse due to biaxial compression loading:* This occurs when the plate is subjected to biaxial compressive loading where the yielding occurs at the intersection of the plate and the stiffeners.
- *Beam-column interaction collapse:* This occurs when the plate and the stiffener at mid-span reach the ultimate strength. This will happen when the strength of the stiffeners is not extremely strong or weak but in between.
- *Collapse due to buckling of stiffener webs (local buckling):* This occurs when the stiffener itself buckles under the compressive load and fails locally, causing yielding of sections attached to the stiffeners.
- *Collapse due to tripping (flexural-torsional buckling) of stiffeners:* This occurs when the stiffener not only buckles locally under the compressive load but also twists; also known as lateral torsional buckling.
- *Collapse due to overall (gross) yielding:* This occurs when the plate section, the stiffened panels, the longitudinal girders, the transverse stiffeners and the longitudinal stiffeners all reach yielding at the same time. Local or overall buckling in this case does not occur until each of the sections reach their yield point. This failure mode usually occurs when the panels are thick and stocky.

Paik and Duran conclude that the ultimate strength characteristics of the aluminum alloy 5083-H116 as compared to the aluminum alloy 5383-H116 are very similar. The failure characteristics did not differ tremendously despite the differences in the mechanical properties in both the parent material and the HAZ.

1.3 - General behavior of aluminum structures exposed to elevated temperatures

The use of aluminum alloys as a structural building material has increased exponentially in the past decade. While aluminum has many advantages such as its lightweight and corrosion resistance one of its main disadvantages is whether it has the ability to withstand elevated temperatures. In general, due to its high thermal conductivity and low melting temperature (580°C - 650°C), aluminum material is extremely susceptible to deformations associated with high temperatures. Therefore, it is imperative that the thermal behavior of aluminum must be included in fire sensitive designs. Currently, there are many resources available which discuss the behavior of aluminum alloys at room temperature but there are few resources which discuss their behavior at elevated temperatures [13].

For extreme fire situations, such as hydrocarbon fires, unprotected aluminum can reach a critical temperature in a short time period of a few minutes [14]. It is important that structural designs with aluminum materials use this type of information to compensate with ways to protect the structure, such as insulation [15]. For example, aluminum plate girders, mainly loaded in shear, are often found in ship structures. In this type of environment, accidental fires can cause these girders to degrade quickly which can also cause harm to the other structures around them [14]. There are two main significant effects of fire on aluminum structures. First, aluminum alloys experience large degradations in the strength and stiffness when exposed to elevated temperatures. Second, due to aluminum's high thermal conductivity, thermal deformations can cause stresses to form within the material [15].

1.3.1 General response of steel vs. aluminum structures at elevated temperatures

A majority of design codes for aluminum at elevated temperatures are created with the knowledge of how steel and other metals act at elevated temperatures. It is therefore important to understand in what ways steel acts similarly to aluminum and in what ways steel acts differently than aluminum. Like aluminum, steel's strength and stiffness degrade significantly when exposed to elevated temperatures. The elastic-plastic assumption used for steel at ambient temperatures can no longer be used when the material is exposed to high temperatures; the stress-strain curves become extremely non-linear [16].

To put these ideas into perspective it is useful to compare the general response of aluminum exposed to elevated temperature to steel. Walker and Tahan [17] present stress-strain curves which reveal that the material properties for aluminum at room temperature are similar to the properties for steel at about 300°C. They extend this analysis by comparing two bridges exposed to elevated temperatures; one made of aluminum and the other of steel. The heat requirements of the bridge are twofold: heat flux of 16 kW/m² on the platform (non-engulfed case) and a "sea pool fire" under the bridge (engulfed case). The bridge is required to be able to withstand both of these cases for a minimum period of time of an hour. The response of the bridge as a whole is first analyzed and then the response of a typical steel panel of the bridge is compared to the response of a corresponding aluminum panel.

Walker and Tahan point out that the rate of temperature increase in the steel members for the bridge will be almost five times faster than that of aluminum. This is due to aluminum's low

emissivity (around 0.2). During the non-engulfed case with the incident heat flux of 16,000 W/m² K after an hour, the aluminum members only reach about 41°C while the steel member reaches about 171°C. For the engulfed case, which is supposed to simulate a pool fire on the sea, the temperature of the aluminum members reach about 79°C after five minutes, while the steel member reaches about seven times that. After an hour of exposure both the aluminum and steel bridges would have failed, but this is an extreme case. Walker and Tahan next discuss the bridge panel responses for both materials. For the engulfed case after five minutes the aluminum panel reaches about 300°C while the steel panel reaches about 750°C. For both materials, the same proportion of strength is lost after five minutes. After an hour the aluminum panel has completely failed and melted while the steel panel is still standing and has only increased its temperature by a few degrees.

From the above results, it can be concluded that aluminum, when exposed to non-engulfed conditions, will survive longer than steel members, primarily as a result of aluminum's low emissivity as compared to steel. Otherwise, if aluminum is exposed to engulfed conditions the aluminum members will not survive as long as steel members. Steel's melting temperature is much higher than that of aluminum which is one of the main reasons why in engulfed conditions steel members will survive longer [17].

1.3.2 Degradation of stiffness/strength properties

Faggiano et al. [15] describe the degradation of five material properties (elastic modulus, yield strength, ultimate strength, ultimate strain, and hardening) for different aluminum alloys when exposed to elevated temperatures.

Generally, aluminum alloys melt at around 600°C but also lose about half their strength at around 200°C [15]. Faggiano et al. presented the yield strength versus the temperature for different aluminum alloys. It is apparent that the alloys which are work hardened (H) and the alloys that are heat treated (T) lose about half their strength at a lower temperature than the alloys that are in their annealed (O) state. At about 250°C, the H and T alloys have lost about 70-80% of their strength, while the O alloys have only lost about 40-50% of their strength. Also, the elastic modulus does decrease as the temperature increases but does so independently of the type of aluminum alloys.

Faggiano et al. also presented a plot which depicts the ultimate strength versus the temperature. The aluminum alloys of type H and T tend to have much larger ultimate strengths than alloys of type O but only up to temperatures of about 100-150°C. Also, for all aluminum alloys it is apparent that the ultimate strain value (which is related to the strain hardening effect) experiences an increase in value as the temperature increases. The value begins to increase more significantly when the temperature reaches about 200-250°C. Finally, the aluminum alloys which are of type O begin with a higher hardness value than the other alloys, however, as the temperature increases the hardness value decreases. The other alloy types, H and T, both experience an increase in hardness generally when the temperature reaches about 200-250°C.

1.3.3 Effect of creep on thermo-structural response of aluminum exposed to elevated temperatures

The behavior of aluminum alloys at elevated temperatures is primarily controlled by a phenomenon termed creep [18]. Creep is generally defined as a time-dependent deformation. This becomes apparent in metals such as aluminum and steel at elevated temperatures. In the analysis of aluminum structures, it is imperative that the effects of creep at elevated temperatures be included. If these effects are not included, results can be extremely nonconservative thus reducing the usefulness of the simulation/model. Specifically, if the model does not include these elevated temperature creep effects the material will act as though it is stiffer than it really is and will ultimately have lower deflection results [19]. In order to investigate the effects of creep in aluminum further it is important to first discuss the three stages and the physical mechanisms associated with creep.

There are generally three stages to creep deformation: the primary or transient stage, the secondary or steady-state stage, and the tertiary or unstable stage. When loads are applied, the initial increase in strain is a combination of the elastic and plastic response. Over time the strain increases in a manner shown below in Figure 3 as a result of creep.

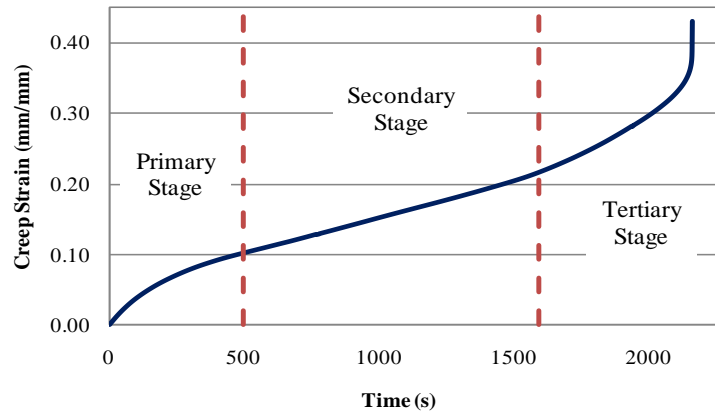


Figure 3. Creep strain vs. time curve – reproduced from [23] with permission of S. Feih, 2011.

The crystal structures found in metals are held together with strong chemical bonds called primary bonds. Crystalline materials or metals have a higher resistance to creep than polymer materials because of these strong primary bonds [20]. There are two main mechanisms of creep that occur in crystalline materials: diffusional flow and dislocation creep.

Diffusional flow is one of the main mechanisms in which deformation due to point defects occur in a crystalline material. Vacancies in the crystal lattice may spontaneously appear along the grain boundary or directly within the crystal grains. High concentrations of vacancies are found perpendicular to the direction of the applied stress within the material. This area with high concentrations of vacancies will move or diffuse to an area with a lower concentration of vacancies either along the grain boundary or within the crystal lattice structure. This creep

mechanism is termed Coble creep if the vacancies move along the grain boundaries and is termed Nabarro-Herring creep if the vacancies move through the crystal lattice [20].

Dislocation creep, also called power-law creep, is one of the main mechanisms in which deformation due to line defects occur in the material. This phenomenon usually occurs at higher temperatures, but can also occur at lower temperatures when diffusional flow is not significant. Dislocation glide occurs when a stress is applied to the material and an edge dislocation is forced to move through the lattice structure. Dislocation climb also describes the same edge dislocation running into obstacles thus forcing that extra plane of atoms to move to a different lattice plane, which is allowed through vacancy diffusion. This phenomenon then allows the edge dislocation to continue to glide, thus both climb and glide become a coupled action [20]. At a specific elevated temperature (dependent upon the type of metal), the power-law creep mechanism breaks down and reaches a transition period where the coupled dislocation glide-plus-climb actions decouple and only dislocation glide is allowed for deformation [21].

Steel and aluminum are both highly susceptible to the effects of creep at high temperatures. Both metals have numerous types of defects in the crystal structure that can either aid or inhibit deformation. The effects of creep deformation become more prevalent as the temperature rises. Kodur and Dwaikat [19] state that most metals begin to experience the effects of creep at a temperature which is about 30% of the melting temperature of the metal.

1.3.4 Curve-fitting raw creep data

In simulations of metals exposed to high temperatures it is imperative to include constitutive properties associated with creep. This generally requires curve-fitting of raw creep data. There are numerous methods to curve-fit creep data. These mathematical models can be time dependent, temperature dependent, stress dependent, or can be a combination of all three [22]. This is entirely dependent on the specific material. The two major mathematical models used to curve-fit raw creep data were contributed by Dorn and Harmathy.

Dorn, in the 1950's, suggested an Arrhenius mathematical type equation which describes the secondary stage of creep. The secondary strain rate was calculated using Dorn's relationship [18],

$$\dot{\epsilon}_{t,II} = Z e^{-Q/RT} \quad \text{Equation 4}$$

where $\dot{\epsilon}_{t,II}$ is defined as the slope of the secondary creep strain region and Z is the Zener-Holloman parameter which is calculated using the relationship,

$$Z = A(\sinh(\alpha\sigma))^n \quad \text{Equation 5}$$

Shortly after, Harmathy expanded upon Dorn's power law relationship to include both the primary and secondary stages of creep [18],

$$\dot{\epsilon}_{t,I+II} = \dot{\epsilon}_{t,II} \coth^2 \left(\frac{\dot{\epsilon}_{t,I+II}}{\epsilon_{t,0}} \right) \quad \text{Equation 6}$$

where, $\dot{\varepsilon}_{t,I+II}$ is defined as the creep strain rate of both the primary (I) and secondary (II) creep strain regions. The term, $\varepsilon_{t,0}$, is the projection back to zero time of secondary strain curve and is fitted by [18],

$$\varepsilon_{t,0} = D(\sigma)^m \quad \text{Equation 7}$$

The terms A , Q , D , α , n , m are fitting parameters dependent upon the specific material. These are found first by plotting creep strain vs. time curves and finding the secondary strain rate of each curve. Plotting this value against the temperature and stress will give the A , α , n , and Q values dependent on both temperature and stress. Plotting the projection back to zero time of the secondary creep strain curve against stress will reveal the D and m parameters which are dependent only upon stress. Equation 6 may be integrated to reproduce creep strain vs. time data using the above equations,

$$\varepsilon_{t,I+II} - \varepsilon_{t,0} \tanh\left(\frac{\varepsilon_{t,I+II}}{\varepsilon_{t,0}}\right) = \dot{\varepsilon}_{t,II} t \quad \text{Equation 8}$$

Maljaars [18] expanded upon the work of both Dorn and Harmathy and included the tertiary stage of creep in his modified model,

$$\dot{\varepsilon}_{t,I+II+III} = \dot{\varepsilon}_{t,II} \coth^2\left(\frac{\varepsilon_{t,I+II+III}}{\varepsilon_{t,0}}\right) \frac{\varepsilon_{t,I+II+III}}{\varepsilon_{lim}} \quad \text{Equation 9}$$

Maljaars [18] created finite element simulations of aluminum alloys 5083-H111 and 6060-T66 which incorporated both the existing and modified creep models. He concluded that for the aluminum alloy 5083-H111, the inclusion of the tertiary stage of creep in the constitutive model did not affect the results. However, for the aluminum alloy 6060-T66, the inclusion of the tertiary stage did in fact affect the results. This can be attributed to the fact that hardening particles form during the ageing process and cause an early occurrence of the tertiary stage of creep. Therefore, the choice of creep model is directly dependent on the aluminum alloy [18].

Feih et al. [23] examined four other curve-fitting methods: the Lombardi model, the Batsoulas model, the Larson-Miller Parameter (LMP) approach, and Abaqus' time-hardening creep power law. The Lombardi model uses a gradually increasing effective stress instead of a constant applied stress. This allows the model to indirectly account for the progression of strain in the tertiary region. The primary and secondary stages of creep strain is described by

$$\varepsilon_{t,I+II} = -\varepsilon_{t,0} \exp(-\theta_2 t) + \dot{\varepsilon}_{t,II} t + \varepsilon_{t,0} \quad \text{Equation 10}$$

$$\theta_2 = A_{III} \sigma_c^{n_{III}} e^{\left(-\frac{Q}{RT}\right)} \quad \text{Equation 11}$$

The parameters for the secondary strain rate and the creep strain projected back to zero time are the same as in the Dorn-Harmathy model. Feih et al. [23] mentioned that this model did not agree well with transient creep data at low temperatures. Intrinsic to the model, the value of ε_0 increased as the temperature increased, thus predicting higher creep strains at lower

temperatures. Feih et al. [23] concluded that this creep model is not appropriate to include in finite element simulations due to this problem.

The Batsoulas model uses Equation 12 to fit all three stages of creep,

$$\varepsilon(t) = \frac{\sigma}{E} + \frac{\sigma}{(\beta_c \eta_c + K_c)} (1 - e^{-(K_c \eta_c) t}) + \frac{\sigma}{(\beta_c \eta_c + K_c)} (e^{\beta_c t} - 1) \quad \text{Equation 12}$$

Feih et al. [23] found the fitting parameters, K_c , η_c , and β_c , through the use of the minimization algorithm tool called GNUplot. After plotting the natural logarithm of each of the parameters versus both temperature and stress Feih et al. [23] were able to determine the stress and temperature relationship for each of the fit parameters. They found that this creep model showed an overall better prediction of the response of all three creep stages than did the Lombardi model. However, for the stresses and temperatures not directly used in the experimental data, the creep strain data must be interpolated. More experimental data must be performed to refine the relationship between the fit parameters and the stress/temperature before the Batsoulas model can be fully utilized [23].

Feih et al. [23] states that the main advantage to using Larson-Miller approach to curve-fitting raw creep data is the fact that short experimental creep tests, ones with high temperature and stress conditions, can be used to predict creep data at low temperatures and stress conditions. The rate of creep deformation can be calculated by,

$$r_c = \frac{\varepsilon_r - \varepsilon_0}{t_r} = A e^{-Q/RT} \quad \text{Equation 13}$$

A is a fitting parameter, Q is the activation energy of the material, and R is the universal gas constant. The term ε_r is the critical value of strain which is found at the transition from the secondary creep stage to the tertiary creep stage and the term ε_0 is the initial creep strain value at time zero. Feih et al. [23] state that the activation energy, Q , does not depend on temperature or time, only stress, therefore the Larson-miller parameter is only stress dependent. After rearranging equation 10, Feih et al. [23] take the logarithm of both sides and result in the equation,

$$LMP = T(\log t + C) \quad \text{Equation 14}$$

LMP is the Larson-Miller parameter, T is the absolute temperature, t is the total experimental time, and C is a constant. From very low strain levels to levels around 0.4 and different C values Larson-Miller master curves are plotted with the log of stress versus the LMP . Creep strain vs. time data can be recreated using these master curves. However, extrapolation to lower temperatures is only possible if the activation energy for the material is not dependent on temperature [23].

The default creep model in the finite element software, Abaqus [24], is the time-hardening power law,

$$\varepsilon = \frac{A}{m+1} \sigma^n t^{m+1}$$

Equation 15

This power law model only includes the secondary stage of creep. The terms A , m and n are material fit parameters. Specifically, Feih et al. [23] had experimental data which was found at high stress levels and high temperatures. Larson-Miller master curves were utilized in order to extrapolate these fitting constants at lower temperatures. The stress dependency is already included in Equation 15. Experimental data could have been directly used to find these parameters at each desired temperature, but time constraints required the use of the *LMP* approach. Feih et al. [23] found that this method agreed well with the available experimental data.

1.3.5 Current requirements for fire protection

For fire sensitive designs it is imperative to have requirements regulating the amount of insulation or other fire protection materials. According to Sielski [1] the requirements in place do not allow the temperature of aluminum to exceed 200°C above room temperature. However, this is assuming that the ambient temperature is about 30°C; if this is not the case, design requirements need to be modified. In the shipbuilding industry the fire protection requirements vary from the commercial ships to U.S. Navy ships. For example, the commercial ship building industry requires that their ships withstand a small wood fire. The U.S. Navy requires that their ships withstand an oil fuel type of fire which burns at significantly higher temperatures. The insulation required for the U.S. Navy ships will be almost twice as heavy as the fire protection required for commercial ships [1].

1.4 - Previous experimental work and finite element simulations of the buckling failure of aluminum plates exposed to elevated temperatures

The history of using steel as a structural material far surpasses that of aluminum. The majority of design rules for aluminum were at one point associated with the design rules for steel. The material properties for aluminum and steel are different in so many ways thus design codes for steel structures may not always be appropriate for aluminum structures. One difference, for example, is that the material properties of aluminum alloys degrade significantly when exposed to elevated temperatures. Current design codes for aluminum do not completely cover this important subject [25]. Among the numerous failure mechanisms of aluminum structures, one of the most affected by high temperature exposure is local buckling [26].

Local buckling is an important topic to cover because when this type of failure occurs in a structural component as a result other members surrounding it can weaken significantly. Studies have been done in the past concerning the local buckling of aluminum at ambient temperature but there are few studies in the literature that investigate local buckling of aluminum members at elevated temperatures. The local buckling of aluminum at room temperature is greatly dependent on aluminum's material properties, such as the yield stress, the proportional limit, and Young's modulus. A low value of the ratio of the proportional limit over the yield stress points to a low critical buckling stress. As the aluminum material is exposed to higher temperatures the buckling stress decreases and the stress-strain properties of the material degrade significantly [26].

1.4.1 Previous experimental work

Langhelle et al. [25] performed experiments which investigated the buckling of aluminum alloys 6082-T4 and 6082-T6 columns. They ran three types of tests: constant load with an increasing temperature, constant temperature with an increasing load, and room temperature buckling tests. Columns with transverse welds along the mid-section of the column were also evaluated. Finally, all of the experimental results were compared to the buckling curves available currently in the design codes. Available design codes use a knock-down value for the material properties of aluminum when exposed to elevated temperatures. This may be acceptable for some alloys but material properties vary from one aluminum alloy to the next. Different tempers of aluminum alloys gain strength, rapidly lose strength, or gradually lose strength when exposed to elevated temperatures.

The columns used in the experiments were 120mm in width, 2100mm in height, and 7mm in thickness. The initial imperfections of the columns were measured: less than 1mm for unwelded columns and less than 2.1mm for welded columns. The end boundary conditions were pinned-pinned and a spherical surface was placed at both ends to ensure this condition. Heating elements were placed strategically around the specimen and then insulation was also placed to reduce the amount of heat lost during the test.

The buckling behavior of the unwelded columns at room temperature was governed by elastic-plastic deformation where the mid-section of the column experienced the most plastic deformation (out-of-plane) before failing. Tests were carried out until the specimen actually

ruptured and broke. The T4 specimen showed much more ductile behavior before rupturing than the T6 specimen. The buckling behavior of the welded columns actually reduced the buckling strength of the T6 specimen (by 23%) and failed in a brittle manner while the buckling strength of the T4 specimen was almost completely unaffected [25].

1.4.1.1 Results of buckling tests at constant temperature rate (constant load increasing temperature):

Two different heating rates were used to determine whether or not creep had any effect on the critical temperatures of the specimens. The unwelded T6 columns showed almost no difference for each of the two heating rates (critical temperature was around 250°C). This may suggest that creep for that certain time period did not have a very large effect. The welded T6 column showed a smaller critical temperature (220°C). This can be attributed to the reduction of the properties in the HAZ at elevated temperatures. The unwelded and welded T4 columns all produced very similar results for the critical temperature (about 290°C). The weld in the T4 specimen had almost no impact in the results [25].

Results of buckling tests at constant temperature (constant temp and increasing load): Creep effects in buckling problems are entirely dependent upon the values of the load and temperature. In the results, significant creep effects are seen at higher loads. Upon the critical temperature the column's out-of-plane displacement increased exponentially until failure. The T6 and T4 specimens showed similar results for the constant temperature tests. This provides insight that the artificial aging process used to create AA6082-T6 is lost during these types of constant temperature tests [25].

Significant differences in experimental results compared to the design code results point to the fact that design codes are limited in their ability to predict failure of aluminum at elevated temperatures. The movement to conduct more tests and create analytical or finite element models to predict failure is necessary in order to revise these codes [25].

Maljaars et al. [26] also ran steady-state and transient experimental tests which investigated the buckling of aluminum columns at elevated temperatures. These tests are then used to validate finite element models described in [27]. Experimental tests become expensive so there are obvious advantages to using finite element software to be able to predict the local buckling failure of aluminum members. The finite element models once validated with experimental data could possibly be utilized to revise portions of the design code which are unclear [26].

Simply supported local buckling tests on square hollow sections (SHS) and angular sections (AS) were also conducted. These sections were used instead of flat plates because they were easier to test in the laboratory. Specifically, for the AA6060-T66, the square hollow section had b/t (width/thickness) ratios of 25, 44 and 60, while the angle section had a b/t ratio of 25. Specifically, for the AA5083-H111, the square hollow section had a b/t ratio of 50 and the angle section had a b/t ratio of 50. The height of all the specimens was 600mm. The dimensions were chosen as such so that local buckling is possible at room temperature for each of the sections. The sections were placed in a furnace to allow for homogeneous temperature distribution around

the perimeter of the specimen. The load cell was applied at the top cross section of the specimen and allowed for movement in the vertical direction and no movement in the horizontal direction. The angle section needed to be “adhesively bonded” to the load cell/supports in order to deform in a simply-supported manner [26].

1.4.1.2 Steady-State test results:

The SHS section of the AA 6060-T66 with a b/t ratio of 25 seems to have almost no difference in the resistance at different constant temperatures. There is only one temperature (179°C) with this section and alloy that slightly reaches above 1.0 which means the specimen reached its plastic capacity for a short period time before it failed. This was the only specimen in all of the tests to achieve this. The AA 6060-T66 SHS section with a b/t ratio of 44 showed a more significant increase in buckling resistance as the temperature increased, though none of the tests reached the ratio of 1.0. The results of the angle section of AA 6060-T66 showed that the buckling resistance of the specimens were all very similar with almost no difference. The SHS section and the AS section of the AA 5083-H111 type seems to only slightly increase its resistance to local buckling as the temperature increases, but does not produce significant differences. This is attributed to the fact that the ratio of plastic capacity to modulus of elasticity at elevated temperatures of the alloy is only slightly lower than that of the alloy at room temperature [26].

1.4.1.3 Transient state test results:

In general for each alloy, the transient state results show that the buckling resistances at higher temperatures are greater than the resistances found at room temperature. This is again attributed to the fact that the ratio of the yield stress (or plastic capacity) to the elastic modulus decreases as the temperature increases [26].

Langhelle et al. [14] ran experimental tests associated with the shear buckling behavior of aluminum plate girders. These aluminum sections are commonly found on ships and are mainly loaded in shear. Two alloys were used in testing: EN AW-5754 H34 for the web material and EN AW-5083 34 for the flanges and end plates. Elevated constant temperature tests were conducted with a 20 minute heating period. Softening of the aluminum specimens occurred for a long period of time before rupture. The results from these tests were presented in the form of load-displacement curves [14].

For the room temperature test, the load reaches a peak around 250 kN and remains constant until about 60mm of displacement is reached. The load then decreases quite rapidly until 80mm of displacement when the specimen failed. The shear buckling can clearly be seen in the room temperature test and after a period of time cracks begin to form in the HAZ region of the welded portion of the girder and the specimen fails shortly after that [14].

The ultimate capacity of the girder at 200°C is about 70% of the capacity of the girder at room temperature. The ultimate capacity of the test at 200°C is reached much sooner than the test at room temperature. Due to the softening affect at elevated temperatures, a displacement of 200mm is reached before failure of the specimen. The capacity of the test at 225°C is also

reached much sooner than the room temperature test and only 100mm of displacement is reached before failure of the specimen. The authors reveal that the temperature in some areas of the specimen may have reached over 250°C so this might have been a factor in the lower displacement value at rupture. From their experimental results, Langhelle et al. [14] concluded that the temperature requirements of aluminum should change from 200°C above ambient temperature to 200°C [14].

1.4.2 Previous work – finite element simulations

Maljaars et al. [27] used the experimental results found in [26] to validate finite element models. They used the finite element software, DIANA, to run simulations of the test sections exposed to fire conditions. They used shell elements (S8) which have 8 nodes for each element. The models have 10 elements for the width and 54 elements for the height of the sections. The authors increased the mesh density by two and found the results to be within 1 percent of the original results, therefore they found no need to run models with higher mesh densities [27].

Geometrical imperfections were also included in the models to obtain more accurate results. These were measured in most specimens but in some a nominal imperfection value was used (0.1mm in the AS of 5083-H111 specimens). The boundary conditions of the specimen in the finite element model were created using surface interface elements at each end of the specimen (contact elements CL12I). These elements were given extremely high stiffness values in the axial direction so as not to influence the results of the aluminum local buckling. Thermal expansion was not incorporated into the models. However, the residual stresses in the welded sections were applied in the models with the constitutive properties of the welded material equal to that of the parent material. Due to creep the residual stresses slowly relax during the testing and the materials becomes more ductile [27].

It is essential to include detailed material properties in finite element models. Without accurate constitutive models, finite element simulations are useless. Maljaars et al. [27] used elastic and plastic material properties as well as creep properties to describe their material properties. They also included thermal properties in the model such as density, specific heat, and conductivity. The creep model is based on all three stages of creep (primary, secondary and tertiary stages).

Upon comparison of test results and finite element results Maljaars et al. concluded that it is possible to accurately predict the buckling failure of aluminum columns exposed to elevated temperatures.

Langhelle et al. [14] also created finite element models of the shear buckling behavior of aluminum plate girders. They ran models using Abaqus and another program called USFOS. Two different models were created; one which included the reduction in material properties in the HAZ and one which did not. The model at room temperature without the HAZ affect compared well with the test data. However, at elevated temperatures the models without the HAZ affect over-predicted the experimental data. After the 20% reduction in strength was applied to the HAZ, the results compared very well. The aluminum design code, which uses the tension field theory, generally over-predicted the ultimate strength of the aluminum girders at

elevated temperatures. At 200°C the code moderately over-predicted the ultimate strength and as the temperature increased to 225°C the code significantly over-predicted the ultimate strength of the girder [14].

1.5 - Previous work using strength reduction (knock-down) factors to model welded aluminum material in finite element simulations

Users of finite element programs have the ability to create and change models with ease. For example, Roper and Burley [28] created finite element models of welded beam/column joints. They investigated the effects of using different materials in the welded section of these models. Users of finite element programs have the ability to separate entire models into different sections which can carry different material properties [28].

Dobmeier et al. [29, 30] investigated the structural performance of an aluminum bridge deck made of aluminum alloy 6063-T6. The authors created a finite element model to compare with experimental data for both service performance loads and failure type loads. Recently, in the past decade, interest arose in using aluminum as a bridge deck material due to its lightweight. Another advantage to using aluminum as a bridge deck material is, as mentioned before, the substructure of the bridge does not have to be changed. Specifically, the extruded cross section of the bridge deck is depicted in Figure 4 below. Figure 5 reveals the extent of the large-scale bridge deck [29].

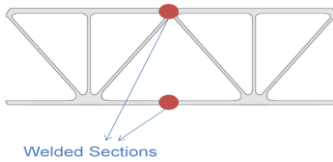


Figure 4. Extruded cross section of bridge deck reproduced from [29] with permission of J. Gomez, 2011.

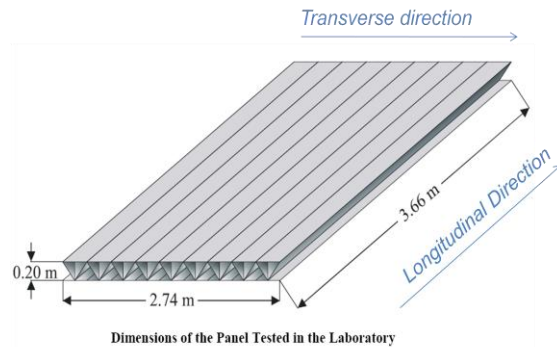


Figure 5. Large-Scale extent of bridge deck reproduced from [29] with permission of J. Gomez, 2011.

The shell models of the bridge deck were created using Abaqus. Simply supported boundary conditions were created along either the transverse or longitudinal directions depending upon the experimental setup. Also, vertical stresses were applied using a distributed pressure load in the areas specified experimentally. Shell elements were used instead of solid elements for ease of calculations. In the first section [29] the service load performance was evaluated where stresses were applied to the model which acted as a typical tire load on a highway. In the second section [30] failure performance was evaluated through the application of large stresses until the deck ruptured. In section [30] the model included welded sections (in between the extrusions as shown in Figure 6 which were partitioned in Abaqus and were given a

knock-down averaged yield stress value. This method takes a reduced yield stress value (found experimentally or averaged) and applies it to a region that is one inch on either side of the weld centerline. Dobmeier et al. [30] then applies this reduction in yield stress to the partitioned welded regions in Abaqus. Unfortunately, Dobmeier et al [30] do not further partition the welded region into multiple reduced yield stress zones. This could possibly lead to more accurate results.

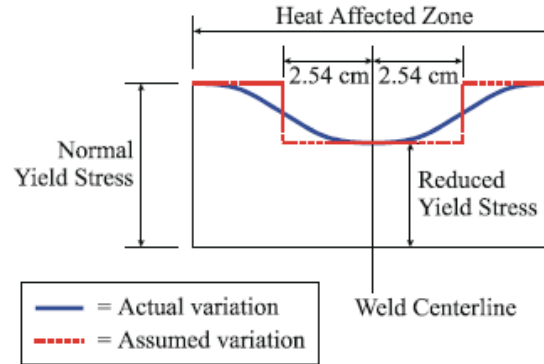


Figure 6. Knock-down method reproduced from [29] with permission of J. Gomez, 2011.

The comparison of the finite element model results and the experimental results reveal that the models slightly over-predicted the stiffness of the bridge deck and thus gave slightly conservative results, but overall the experimental and model results agreed well. Dobmeier et al. [30] did not run a convergence study on the mesh of the models in Abaqus. This also could have led to an even better agreement between the model and experimental results.

Vaughan and Schonberg [31] also used this type of method to reduce material properties in the HAZ of two aluminum materials butt-welded together. The Abaqus finite element model for the welded region consisted of 16 elements from the top of the weld to the bottom of the weld. Vaughan and Schonberg [31] seem to be fully confident in their mesh density. The experimental stress-strain data were obtained from tensile tests that were taken at certain points in the welded and parent material. These points were then linearly interpolated so that there would be a smooth transition of material properties from element to element in the finite element model [31].

Results showed that stress-strain values from Abaqus agreed well with experimental data along the direction of the load, or the longitudinal direction. Along the y-direction at the top of the weld the results seem to agree well with experimental direction. However, along the y-direction at the bottom of the weld the results seem to diverge and over-predict the stress at around 138 MPa when the deformations became permanent or plastic. Also, along the z-direction at the center of the weld, the model results agree well with the experimental data but only for the linear elastic region of the deformation response. Once the yield stress is reached the model results begin to diverge from the experimental results and over-predict the stress-strain response. Vaughan and Schonberg [31] attribute this to the fact that Abaqus relies on the assumption of constant volume deformation for plastic deformations. The constant volume deformation assumes a plastic contraction ratio of 0.5. This ratio is the absolute value of the plastic strain in

the z direction over the plastic strain in the y direction. The experimental data show that after yielding occurs this value increases beyond the value of 0.5. They explain that this is due to the fact that there is much more deformation in the y-direction than in the z-direction and this is mainly due to residual stresses formed during the welding process [31].

In the previous work described in this section, reduction of yield stress values in finite element models seemed to show acceptable results as compared to experimental data. It does seem, though, that residual stresses may play a role in certain aluminum structural applications and should be incorporated into finite element models to obtain refined results.

1.6 - Discussion

The use of aluminum as a structural material has many advantages but like any material it also has its disadvantages. Among the advantages are its lightweight and its excellent corrosion resistance. Among its disadvantages is its degradation of mechanical properties (such as elastic modulus and yield strength) when exposed to elevated temperatures. Thus, in order to implement aluminum as a structural material, extensive research is required to understand the ability of aluminum to withstand elevated temperatures.

Countless investigations in the response of steel structures exposed to fire have been conducted over the years. Investigations concerning the response of aluminum exposed to fire are few and far between as compared to the extensive knowledge of the response of steel. Current aluminum fire design codes use the vast knowledge of steel structures to create design formulations. This may in some designs be accurate but in others may not. Extensive research is needed in this field to improve the accuracy of aluminum design codes.

The use of finite element simulations of aluminum structures exposed to fire will provide an outlet where experimental parameters can be varied quickly and easily. Finite element simulations allow any component of the structural model to be modified in order to understand its impact to the entire structure. These modifications are not made as easily experimentally. Before these simulations can be used, however, extensive experimental data is needed in order to validate these finite element models. Once there is confidence in these models they can be extended to more complicated structural/components.

Chapter 2 – Validation of intermediate scale buckling tests of one-sided heating of 5083-H116 aluminum plates

2.1 - Introduction

In recent years, aluminum has become accepted as an alternative to more widely known structural materials, such as steel. Evidence for this exists in a great number of marine applications as well as in bridges which could range from footbridges to traffic bridges. Advantages that lead to this greater utilization of aluminum include the fact that aluminum has a lower dead weight than conventional structural materials as well as a better ability to resist corrosion. The maintenance costs associated with aluminum are therefore much less than other structural materials [4]. This growing interest in the use of aluminum as a primary structural material has led to questions of its ability to withstand high temperatures. Information regarding the behavior of aluminum under fire conditions is very limited due to the difficulty in predicting aluminum's thermo-structural response at elevated temperatures [15]. Due to this difficulty, finite element programs can be used as a validation tool for both complicated analytical techniques and experimental techniques. The aim of this study is to be able to characterize the thermo-structural response of 5083-H116 aluminum plates under a constant applied compression stress and one-sided heating, and to predict those results using the finite element method.

2.2 - Experimental Characterization

Large-scale tests (with dimensions on the order of meters) are those in which a large portion of a structure is tested, while small-scale tests or coupon tests (with dimensions on the order of a few millimeters) can be done in a small laboratory. The small-scale tests are typically conducted in order to determine material properties, while the large-scale tests are designed to develop the influence of material properties on structural response. However, these large-scale tests are quite expensive to run. Intermediate scale tests (tests conducted on samples that are roughly a meter in dimension) offer an attractive compromise: they are small enough to be run quickly in a laboratory, and yet large enough to elicit structural response. In the intermediate-scale tests for this effort, plates of 5083-H116 aluminum 205mm wide, 865mm in length, and 6-9mm thick were tested. During these intermediate-scale tests, the aluminum plates were clamped on both ends and held vertically in a load frame. Hydraulic jacks located directly beneath the frame allow for a compressive stress to be applied vertically upwards on the bottom of the panel. Directly in front of the load frame is a heater panel system which is pushed forward towards the front side of the aluminum panel to apply a constant heat flux during the test. Thermocouples and deflection gauges are placed systematically on the backside of the panel to measure the temperature distribution and in-plane and out-of-plane deflection of the panel throughout the tests. The experimental setup can be seen in Figure 7 [32].

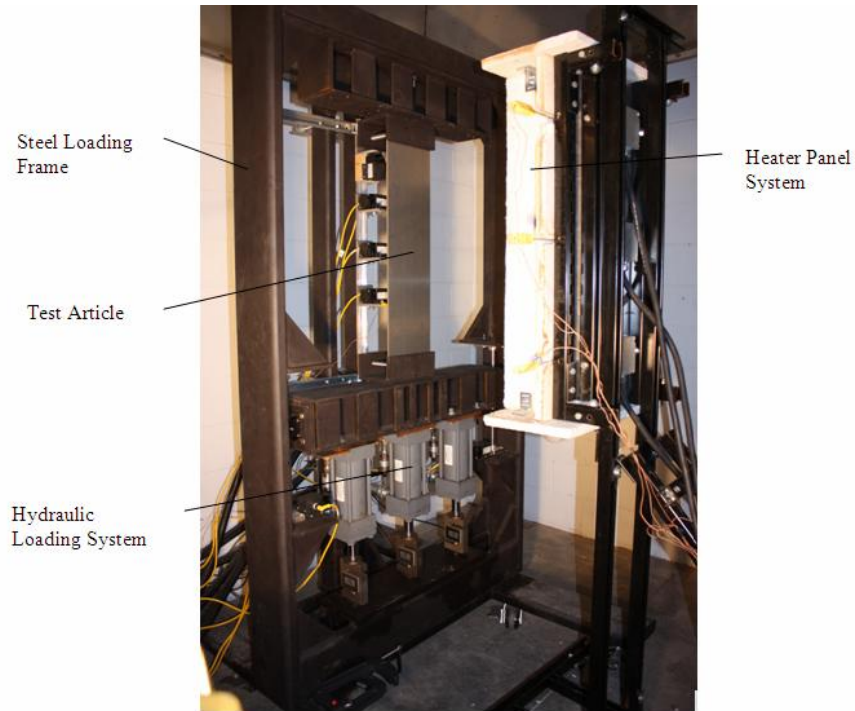


Figure 7. Intermediate scale tests experimental setup, photo by author, 2011.

Tests were carried out until failure of the specimen indicated by the inability of the plate to sustain a compressive load occurred. Fifty-four different tests were conducted in which thickness, applied compressive stress, and heat flux were varied. Thicknesses of 6mm, 8mm, and 9mm were investigated, with applied heat fluxes of 8, 19, and 38 kW/m². In addition to these tests, tests were also conducted in which insulation was attached to the exposed surface with aluminum pins/caps or stainless steel wire. Additional details regarding the experimental procedures are available in reference [32].

2.3 – Building the Finite Element Model

2.3.1 – General Description of the Model

In order to numerically simulate the experimental results, three-dimensional solid and shell models were created using Abaqus. Each of the models has the same vertical length and horizontal width, 865mm and 205mm respectively. Three different thicknesses were used; 6mm, 8mm, and 9mm (corresponding to the experimental thicknesses). To simulate the clamping region, thermally insulated, mechanically fixed boundary conditions were applied over 65mm on either end of the model. Shell elements (4-noded thin conventional shell elements, S4T) were the primary element chosen for the finite element models. In addition, selected models were run in which 3-D continuum 8-noded full integration elements, C3D8T, 3-D continuum 20-noded quadratic full integration elements, C3D20T, 3-D continuum 20-noded quadratic reduced integration elements, C3D20RT, and 3-D continuum 8-noded reduced integration elements, C3D8RT, were used. After acquiring numerous results from these models, a mesh convergence study was completed for both solid and shell models. In addition to the element types used above, selected models were run with quadratic (8-noded) reduced integration thick shell elements, S8RT, and continuum 8-noded reduced integration shell elements, SC8RT. The results, in certain cases, experienced significant changes and provided insight into what phenomena caused these changes.

2.3.2 - Description of Abaqus Shell and Solid Elements

Solid elements are one of the most commonly used elements in finite element analysis. For bending problems, C3D20 or C3D20R elements are highly recommended, but C3D8 and C3D8R can also be used. The specific description for each of the solid element types are listed below:

- C3D8T: An 8-node thermally coupled brick, trilinear displacement and temperature
- C3D8RT: An 8-node thermally coupled brick, trilinear displacement and temperature, reduced integration, hourglass control
- C3D20T: A 20-node thermally coupled brick, triquadratic displacement, trilinear temperature
- C3D20RT: A 20-node thermally coupled brick, triquadratic displacement, trilinear temperature, reduced integration

However, linear solid elements both reduced integration and full-integration, experience two types of phenomena termed hourglassing and shear locking respectively. These can be detrimental to the accuracy of finite element predictions and must be handled accordingly.

Due to the effects of hourglassing, linear reduced integration elements are sometimes not recommended for bending simulations. Linear reduced integration elements use only one integration point in gauss-legendre quadrature. Specifically, the stresses (shear and normal) have

zero value at this integration point thus energy is not produced in the model after elements deform. This causes the elements to act overly flexible and occurs when a coarse mesh is used [33]. Most finite element programs try to compensate for this effect by using an hourglass control option. Specifically, in Abaqus, there are options which can compensate for this hourglassing effect. Abaqus automatically sets the hourglass control to a default setting which adds in a certain amount of artificial strain energy to provide stiffness to the model. There is also an option which sets the hourglass control to an enhanced setting. This options adds slightly more artificial strain energy than the default setting. These two options are shown in the results portion of this thesis.

The phenomenon termed shear locking may also cause numerical problems for bending analyses in finite element programs. This phenomenon is mainly seen in 3-D continuum linear full integration elements. Sun [33] explains that under a bending moment an element should deform in a curved manner. However, a linear fully integrated 8-noded element will not behave this way. These elements experience a tensile stress on the top surface and a compressive stress on the bottom surface (or vice versa) therefore the internal angles are forced to change from 90 degrees. This angle change is due to an inaccurate shear stress that has been introduced. Therefore, the strain energy of the linear fully integrated elements is producing shear rather than bending. These elements end up locking into each other and significantly over predict the stiffness of the entire model. This phenomenon can be seen in Figures 8(a) and 8(b) below.

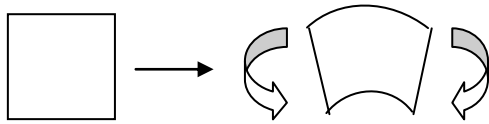


Figure 8. (a)

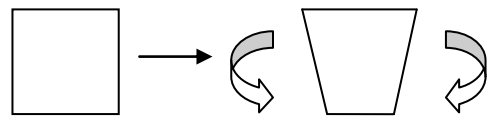


Figure 8. (b)

- (a) curved deformation of a quadratic element under a pure bending moment
- (b) shear deformation of a linear element under a pure bending moment as a result of shear locking

For linear fully-integrated solid elements, shear locking has a significant effect on bending deformation models where the element aspect ratio of the elements is not considered in the mesh discretization. For example, in Figure 9(a), the linear fully-integrated solid element has a very small thickness as compared to its length and width. In Figure 9(b), the length, width, and thickness of the element are equal. In order for linear fully-integrated elements to provide accurate predictions in a bending deformation model, the element aspect ratio must be a key consideration.

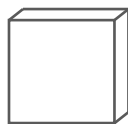


Figure 9. (a)

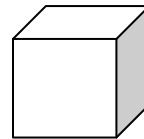


Figure 9. (b)

- (a) linear solid element with poor aspect ratio
- (b) linear solid element with excellent aspect ratio

In the results section of this paper, buckling models (C3D8T elements) with poor and excellent aspect ratios are compared to visualize the effects of shear locking.

Shear locking is not prevalent in quadratic fully integrated 20-noded elements because the elements are able to deform correctly under the bending deformation [33]. After a well-developed mesh (considering element size and aspect ratio) is chosen for the C3D8T elements results should converge or compare extremely well to C3D20T or C3D20RT element results. The advantage, however, of using linear solid elements as opposed to quadratic elements is the total run time of the finite element model. The typical linear solid model reported in this thesis takes about 1-2 hours to complete its analysis, while the typical quadratic solid model takes about 3-5 hours to complete its analysis.

There are numerous shell elements that are available in Abaqus. Plane stress rather than plane strain is used in the shell element formulation; this means that one of the principal stresses (rather than principal strains) is fixed at zero. Three types of shell elements are used in the models presented in this paper. The first is a general purpose shell element, S4. The second shell element type is the S8R, which is a thick shell element. The third shell element type is the SC8R, which is a continuum shell element [24]. The specific description Abaqus output including each degree of freedom for each shell element is listed below:

- S4T: A 4-node thermally coupled doubly curved general-purpose shell, finite membrane strains
- S8RT: An 8-node thermally coupled quadrilateral general thick shell, biquadratic displacement, bilinear temperature in the shell surface
- SC8RT: An 8-node thermally coupled quadrilateral in-plane general-purpose continuum shell, reduced integration with hourglass control, finite membrane strains

The general purpose shell elements (S4) are used in Abaqus finite element models with either thin or thick cross sections. These elements are used predominantly in bending analyses which is the main type of deformation investigated in this thesis. Because the aluminum plates presented in this paper are relatively thin (on the order of 6-9mm) shell elements are a good substitute for the solid elements. The thick shell element (S8R) is an 8-noded quadratic general purpose shell element. These are used again most commonly in bending applications but can also lead to more accurate predictions in applications where transverse shear deformation is significant. These S8R elements have the ability to capture this deformation more closely than do S4 elements. The SC8R elements are found to be appropriate for nonlinear analyses due to their allowance of large rotations and membrane deformations. These elements are first discretized using an extruded solid section and then assigned a shell section within the Abaqus input file [34].

2.3.3 - Mesh Discretization

The number of elements along each geometrical direction is described in Table 1 prior to the completion of the mesh convergence study. The solid model has about 12,000 total elements and the shell model has about 900 total elements and three integration points through the thickness.

Table 1. Mesh discretization prior to mesh convergence study

Element Type	Thickness (mm)	No. of elements along length	No. of elements along width	No. of elements through thickness
<i>Solid</i>	6,8, and 9	60	20	10
<i>Shell</i>	6,8 and 9	60	20	3 (integration points)

A graphic of the plate and its orientation as well as a close-up of the mesh through the thickness of the 3-D solid model is shown in Figures 10(a) and (b) respectively.

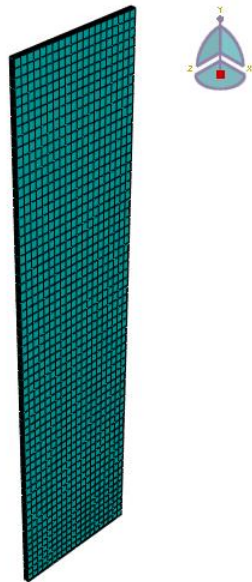


Figure 10. (a)

(a) Graphic of Mesh Discretization

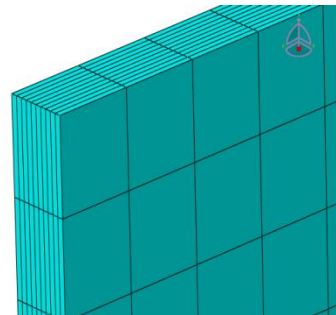


Figure 10. (b)

(b) Close-up of mesh through thickness

The number of elements along each geometrical direction is described in Table 2 following the completion of the mesh convergence study. The final solid model has 76,800 total elements for 8mm and 6mm thick plates and 102,400 elements for 9mm thick plates. The final shell model has 6,400 total elements with three integration points through the thickness. Figure 11 depicts a close-up of the solid mesh following the completion of the mesh convergence study of the solid elements in an 8mm thick plate.

Table 2. Mesh discretization following the mesh convergence study

Element Type	Thickness (mm)	No. of elements along length	No. of elements along width	No. of elements through thickness
<i>Solid</i>	6.35	320	80	3
<i>Solid</i>	7.94	320	80	3
<i>Solid</i>	9.53	320	80	4
<i>Shell</i>	6,8, and 9	160	40	5 (integration points)

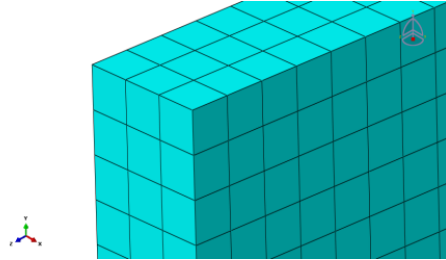


Figure 11. Close-up of elements through thickness – 8mm plate

3.4 - Physical Boundary Conditions

The boundary conditions in the model are defined as fixed because experimentally, the plate is held to the loading apparatus at both ends by grips (65mm in length). As shown in Figure 12, the width of the gripped region is restricted in the x-direction, the length is restricted in the z direction to resist rotation and the bottom face of the panel is restricted in the y-direction.

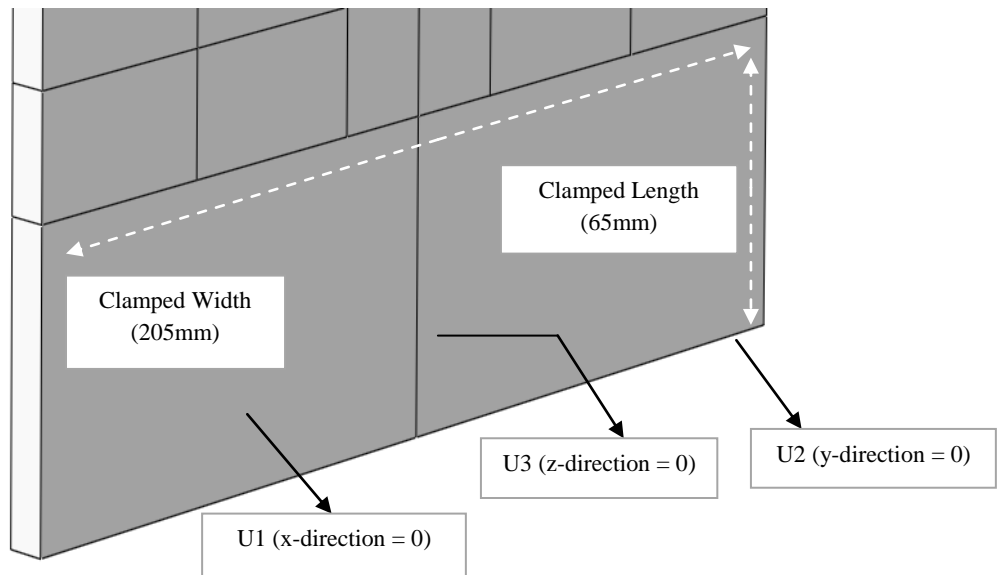


Figure 12. Depiction of fixed boundary conditions on bottom portion of plate

2.5 – Constitutive Properties

2.5.1 - Stress Strain Information

Tensile tests were performed on the 5083 aluminum under isothermal conditions over the temperature range of 25-400°C to determine the softening of the elastic modulus and proof strength. The tensile specimens were dog-bone shaped coupons with a necked gauge section of 8.0mm wide, 10.2mm thick and 600mm long. The specimens were loaded in tension according to ASTM B557 specifications. The specimens were centrally heated over a 100mm section of the gauge region using a temperature controllable heating device. This device prevented heating of the grips and load cell of the tension machine (100kN MTS). Specimens were allowed to equilibrate at the test temperature prior to loading at a cross-head speed of 2mm/min. Typical results are summarized in Figure 13.

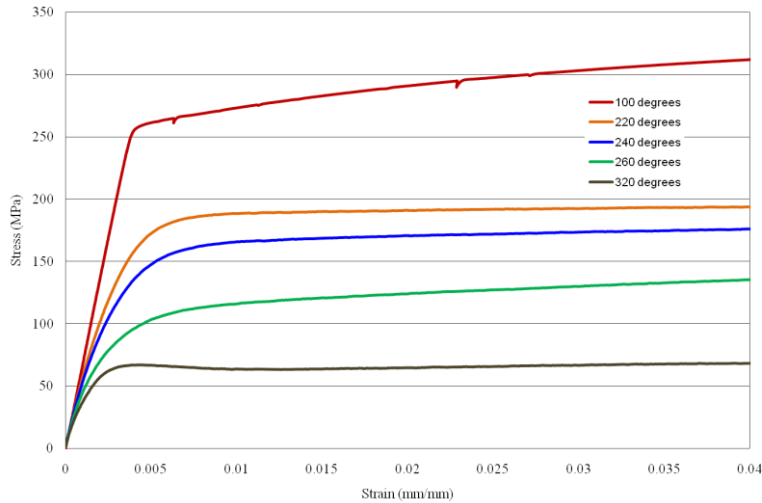


Figure 13. Selected stress-strain curves for 5083-H116 aluminum reproduced from [23] with permission of S. Feih, 2011.

Figure 14 graphically shows the relationship of elastic modulus and temperature and Figure 15 depicts the relationship of 0.2% proof stress and temperature. As seen in both graphs, both the stiffness and yield stress of 5083-H116 Aluminum decreases dramatically when exposed to high temperatures.

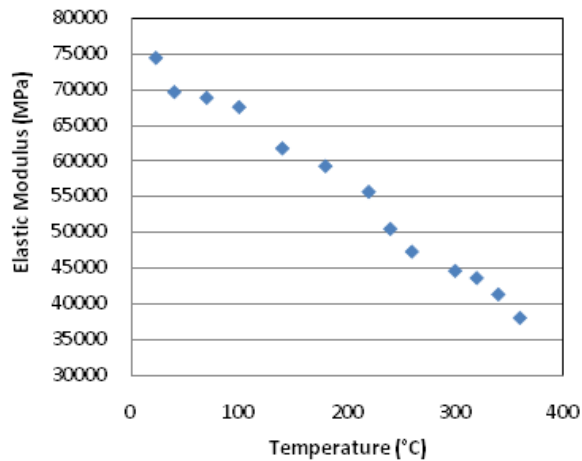


Figure 14. Elastic modulus vs. temperature reproduced from [23] with permission of S. Feih, 2011.

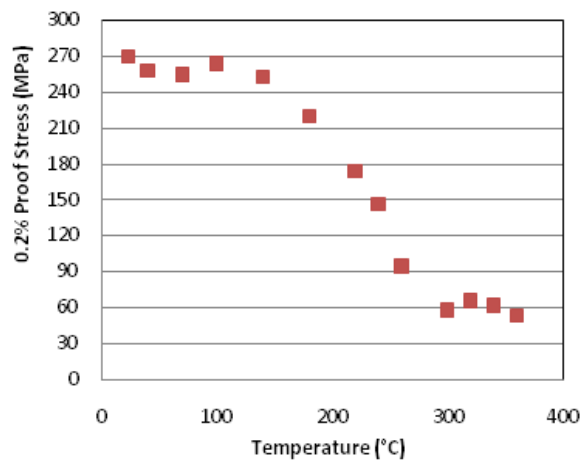


Figure 15. Yield Strength (0.2% offset) vs. temperature reproduced from [23] with permission of S. Feih, 2011.

2.5.2 – Creep Fitting Laws

Isothermal creep tests were performed on the aluminum using the same dog-bone shape specimen as used for the tension tests. The specimens were held at zero stress at the creep test temperature until they reached thermal equilibrium and were then loaded to the creep test stress. Creep tests were performed at constant temperatures between 300 and 400°C and constant stress levels between 50 and 90 MPa. Material parameters describing the primary and secondary creep stages were determined from these tests. Additional details regarding these characterization tests are available in reference [35]. Inelastic softening due to creep is one of the main mechanisms of failure during the fire testing of aluminum plates. The isothermal creep data was represented using the built-in Abaqus power-law creep representation, given by Equation 15, stated in the literature review. The material constants A , m , and n are temperature dependent and can be directly entered into Abaqus. The material constants at varying temperatures are found below in Table 3. This creep model is the default law used in Abaqus. As mentioned in the literature review, there are numerous other ways to model raw creep data in finite element programs through the use of a user subroutine. This law was used because it has been shown to work well in models which have a constant applied stress. The strategies surrounding the choice of creep law will be discussed later in this thesis. Figures 16 through 19 depict the comparison of raw creep data and the calculated creep strain found in Equation 15 for four different applied loads at a constant temperature of 350°C.

Table 3: Material constants for Abaqus creep power law

A	N	m	Temperature (°C)
2.12×10^{-12}	2.14	-0.65	33.4
3.73×10^{-10}	2.14	-0.62	50
1.04×10^{-9}	2.14	-0.56	100
3.20×10^{-9}	2.11	-0.50	150
7.67×10^{-9}	2.14	-0.44	200
2.44×10^{-8}	2.11	-0.39	250
8.94×10^{-8}	2.03	-0.33	300
1.02×10^{-7}	2.11	-0.30	325
1.65×10^{-7}	2.11	-0.27	350
3.74×10^{-7}	2.02	-0.23	375
6.03×10^{-7}	2.02	-0.20	400

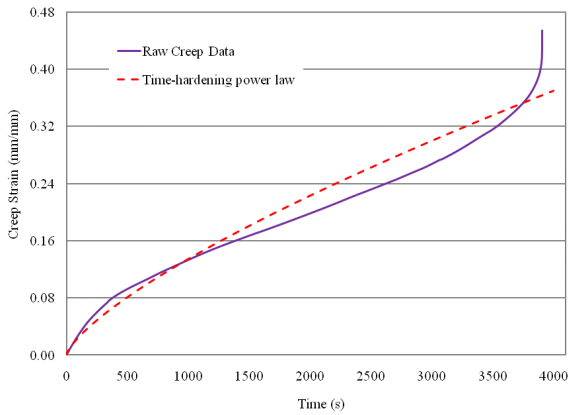


Figure 16. Creep strain vs. time
50 MPa applied stress

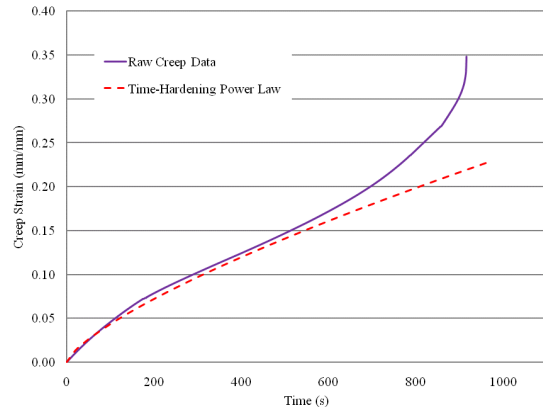


Figure 17. Creep strain vs. time
65 MPa applied stress

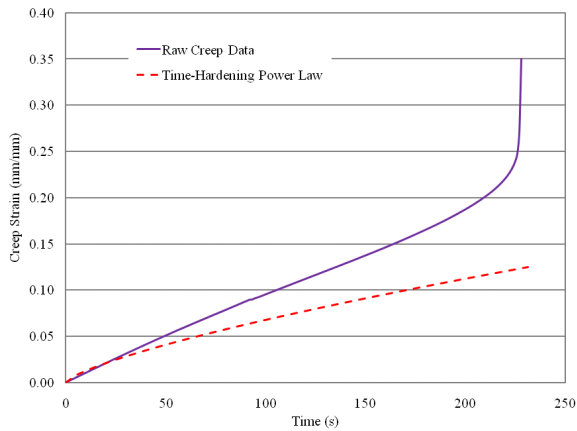


Figure 18. Creep strain vs. time
80 MPa applied stress

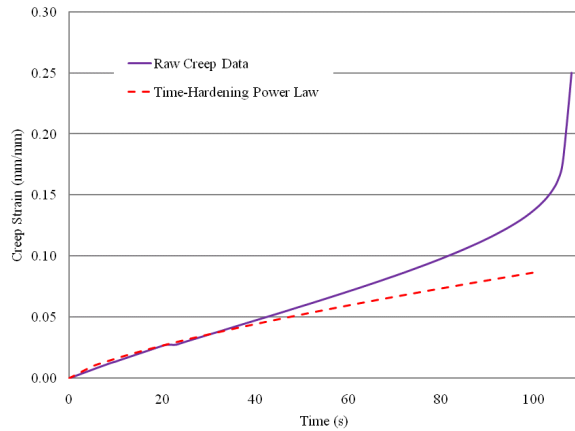


Figure 19. Creep strain vs. time
90 MPa applied stress

The majority of the models presented in this thesis utilize the default power law creep provided by Abaqus. However, a selected set of models were run using an Abaqus user subroutine that utilized the Dorn-Harmathy creep law to curve fit raw creep data. This law not only provides the secondary stage of creep but more clearly defines the primary stage of creep. Equations 4-7 found in the literature review are used to fit the primary and secondary stages of creep (the Dorn-Harmathy creep law). The parameters found in this process do not change with temperature, however, each one of the parameters were found using relationships between temperature and stress. The user subroutine then allows these parameters to be extrapolated based on the specific stress and temperature that is required of the particular model. The parameters are provided in Table 4 below. Also, Figure 20 below shows creep strain vs. time curves for the Dorn-Harmathy creep law compared with experimental data at various applied stresses and a constant temperature of 350°C. Figure 21 below shows creep strain vs. time curves for the Dorn-Harmathy creep law compared with experimental data at various constant temperatures and a constant applied stress of 50 MPa.

Table 4. Dorn-Harmathy Creep Law Material Constants

A	a	N	Q	D	m	R
3.37×10^{-9}	2.19×10^{-3}	5.45	100600	5.67×10^{-2}	0.0	8.314

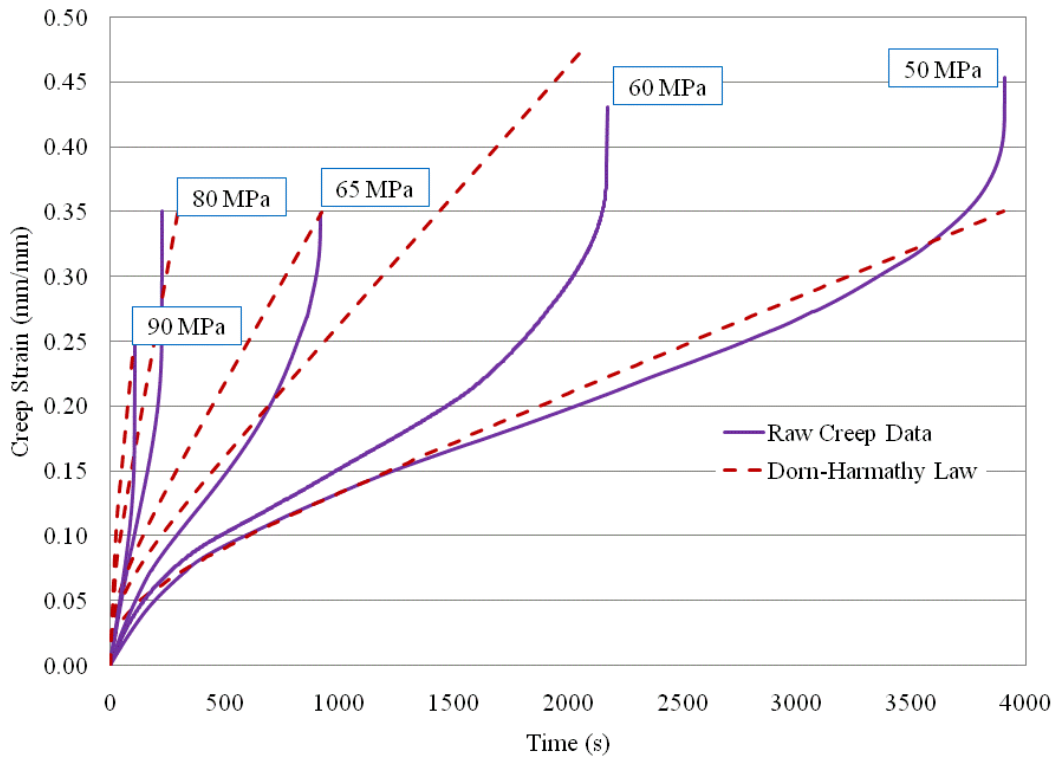


Figure 20. Dorn-Harmathy Creep strain vs. time – various applied stresses at 350°C

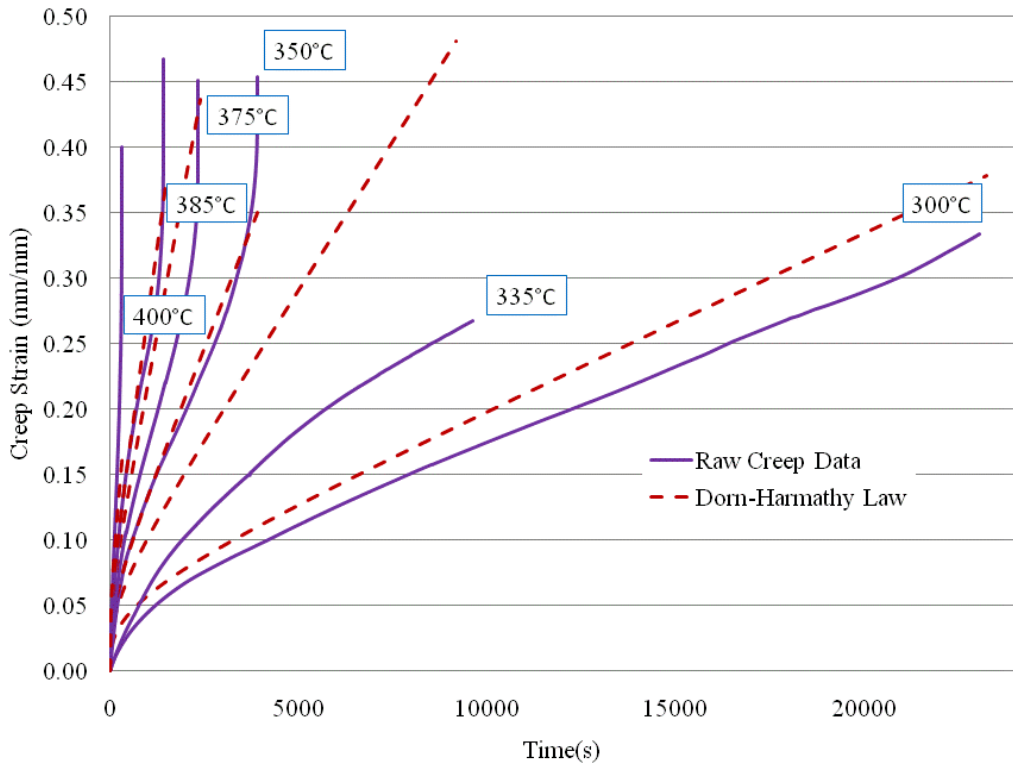


Figure 21. Dorn-Harmathy Creep strain vs. time – various temperatures with an applied stress of 50 MPa

2.6 - Thermal Boundary Conditions

A critical portion of the simulation of the experiments is an accurate representation of the applied heat flux. Heat flux mapping was performed to determine the uniformity of the incident heat flux. Also, a relationship was developed between the heater panel temperature set points and the incident heat flux at the center of the test article. The nominal test article size used in intermediate-scale thermo-structural testing with the compressive load frame had dimensions of 203mm in width and 737mm in exposed height; therefore, the heat flux and velocity mapping were performed over an identical area. The heat flux gage was a Medtherm #64-20SB-19 (Serial #158431) Schmidt-Boelter type total heat flux gage. It has a range of 0 to 200 kW/m² with an accuracy of 3% of the full scale range. The heat flux mapping method used Type-X gypsum board mounted in the mounting clamps to support the heat flux gage. The overall dimensions of the board were 860mm in height and 250mm in width. One-inch holes were drilled in the board in the pattern shown in Figure 7. The heat flux was recorded at each hole location for 60 seconds. The average heat flux over the measurement time was recorded as the heat flux at that location. The heat flux recorded at the center hole location is referred to as the applied heat flux for that given heater panel temperature set point. The locations of the heat flux gauge during this calibration process are shown in Figure 22. Figure 23 depicts the partitioning of the Abaqus simulation model to closely match the heat flux gauge positions and Figure 24 depicts the normalized heat flux across the exposed surface.

To introduce the heat flux boundary conditions into the Abaqus model, Equation 16 below is used. This expression describes the three parts of the thermal boundary conditions used in the models. The first portion of the equation, q'' is the heat flux which is applied to the front surface of the model to mimic the heat source applied experimentally. The second part of the equation describes the surface radiation condition which includes terms such as the emissivity of the surface (ϵ_s), the Stefan-Boltzmann constant (σ), the temperature of the heat flux gage (T_{hfg}) and the surface temperature (T_s). The third part of the equation is the surface film condition (convective term) which includes the heat of convection coefficient (h_{conv}), the temperature of the heat flux gage (T_{hfg}) and the surface temperature (T_s).

$$q'' = q''_{measured} + \epsilon_s \sigma (T_{hfg}^4 - T_s^4) + h_{conv} (T_{hfg} - T_s) \quad \text{Equation 16}$$

The surface radiation was defined on both sides of the panel. The front side was painted black experimentally so its emissivity is input as 0.95. The backside of the panel is assumed to be unpainted so its emissivity is input as 0.2. Each side of the panel is given different values of the convection heat transfer coefficient, h_{conv} . The exposed side of the panel is given the value 15 kW/m²K and the unexposed side of the panel is given the value of 5 kW/m²K. The heat transfer coefficients as well as the emissivities were not measured experimentally therefore these numbers were chosen from a range of values typically found for aluminum. The heat transfer coefficient on the exposed side is given a higher value than on the unexposed side due to the high velocity of the air around within the area exposed to heat. This differential is also due to the slight difference in gas temperature experienced by the exposed and unexposed sides of the plate.

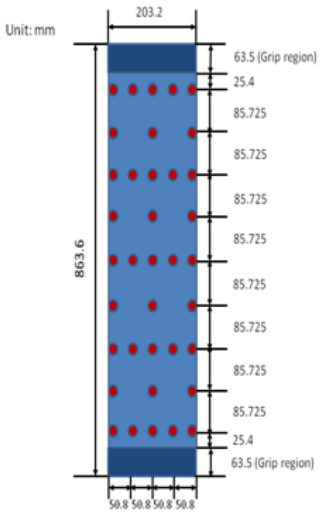


Figure 22. Heat flux gauge locations

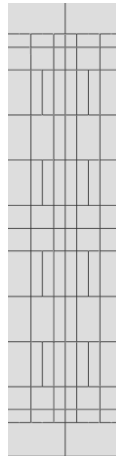


Figure 23. Partitioned model in Abaqus

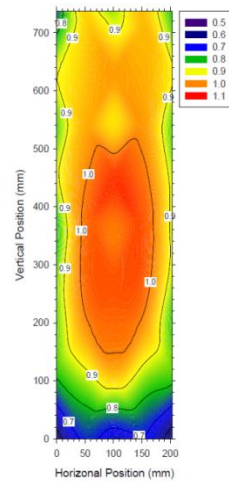


Figure 24. Normalized heat flux pattern

2.7 - Initial Imperfections

The aluminum samples used in the intermediate-scale tests were cut from a rolled aluminum plate. During the manufacturing process, residual stresses may arise resulting in spring-back of the specimens during cutting. The resulting imperfection (non-flatness) has been shown to be of critical importance in predicting the time-to-failure of aluminum samples during one-sided fire exposure under compressive loading. Previous work [36] indicated that the majority of the plates tested experimentally had an initial imperfection within the range of 0.25mm and 1.5mm. The majority of the models were run with an initial imperfection of 1.5mm and a select few models were run with an initial imperfection of 0.25mm to understand the effect this had on the predicted response – both in terms of out-of-plane deflections and predicted times-to-failure.

The first step in implementing these initial imperfections into Abaqus is to complete a linear perturbation, or buckle step in the models for each thickness. During this buckle step Abaqus uses an eigenvalue analysis to determine the critical buckling load (or stress) of the specific plates (6mm, 8mm and 9mm thicknesses). This is also completed for the various types of elements used in the models. In order to obtain the deflections from the completion of this buckle step, the phrase below is used within the input file [36].

***Node File**

U

This results in this .fil file extension includes the deflections (U) in three directions (x, y, and z) at each node. This file is output to the same directory as the buckle step input file.

The next step is to implement this imperfection into the coupled temperature-displacement step models (for each experimental test). The phrase below is used within the new coupled temperature-displacement step input file.

***Imperfection, File=Buckle, Step=1**

1,1.5

“Buckle” is the example input file name used during the buckle step. The 1 specified in the second line is the buckling mode number and the 1.5 is the value of the imperfection in the same units as the buckle step model [36]. Figure 25 below is a flowchart from [36], which shows the entire implementation process of the initial imperfections into the coupled temperature-displacement step models.

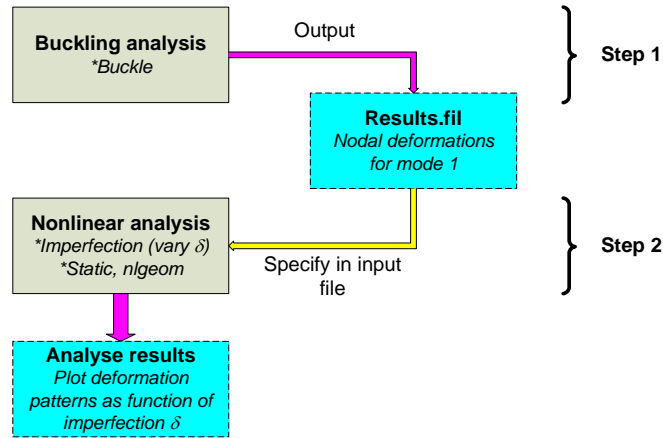


Figure 25. Flowchart of initial imperfection implementation in Abaqus from [36] with permission of S. Feih, 2011.

The predictions presented in this thesis shed light on the ability of finite element models to predict the failure of aluminum plates exposed to fire. The capabilities of these models can then be extended to more complicated aluminum structures that have the possibility of extreme fire exposure. The creation of this model took great consideration in multiple areas; constitutive properties, thermal properties, heat transfer properties, element type, element mesh, as well as geometrical imperfections. Provided that the choices made in these models gave accurate predictions of failure, these concepts should certainly be extended to larger scale models and more complex structures.

2.8 - Results

The section includes numerous studies on the effects of various parameters in the finite element models. Amongst these is the choice of element type of which includes solid elements and shell elements. More specifically for the solid models, this includes continuum solid elements (C3D8T, C3D8RT, C3D20T, and C3D20RT). For the shell models, this includes linear and quadratic conventional shell elements as well as continuum shell elements (S4T, S8RT, and SC8RT). The mesh density was another parameter that was investigated in the models. This specifically includes the choice of a coarse or fine mesh as well as the element aspect ratio. In terms of the heat transfer portion of the models, the effect of emissivity was also investigated. Reference [32] includes experimental results which are compared to the predicted results in this section.

Theoretical buckling loads

The Euler buckling load presented in Equation 17 was used to calculate the theoretical buckling load at room temperature for each plate thickness. This was utilized because of the simple rectangular cross section of the plates. It is much more difficult to calculate a theoretical buckling load with a complicated cross section.

$$P_{critical} = \frac{\pi^2 EI}{(kL)^2} \quad \text{Equation 17}$$

Table 5 below refers to the values of the moment of inertia (I) for each of plate thicknesses, along with each cross-sectional area and critical buckling stress.

Table 5. Moment of Inertia, cross-sectional area, critical buckling stress values

Thickness (mm)	Cross-sectional Area (mm ²)	Moment of Inertia (mm ⁴)	Critical Buckling Stress (MPa)
6.35	1300.4	4369.6	17.04
7.94	1625.5	8534.4	26.63
9.53	1950.6	14748	38.34

The theoretical critical buckling stress is significantly affected by the thickness of the plate; as the plate thickness increases from 6mm to 9mm the critical buckling stress increases to about 20 MPa. As discussed above in the initial imperfection section, a linear perturbation buckle step must be completed before utilizing the initial imperfection in the coupled temperature-displacement model. In this step, the critical buckling load of the section is calculated using an eigenvalue analysis.

2.8.1 - Results prior to mesh convergence study

In order to make conclusions about parameters such as element type and mesh density, aluminum plate models which did not predict failure accurately need to be presented. Table 6 below presents the critical buckling stresses prior to the mesh convergence study for each studied

element type. Table 7 presents the critical buckling stresses following the mesh convergence study.

Table 6. Numerical buckling stresses prior to the mesh convergence study

Element Class	Element Type	Thickness (mm)	Critical Buckling Stress (MPa)
Solid	C3D8	6.35	36.87
Solid	C3D8	7.94	58.66
Solid	C3D8	9.53	58.12
Solid	C3D20	6.35	17.49
Shell	S4	7.94	27.30

Table 7. Numerical buckling stresses following the mesh convergence study

Element Class	Element Type	Thickness (mm)	Critical Buckling Stress (MPa)
Solid	C3D8	6.35	17.92
Solid	C3D8	7.94	27.17
Solid	C3D8	9.53	39.13
Solid	C3D8R	7.94	24.14
Solid	C3D20	6.35	17.45
Solid	C3D20	7.94	27.11
Solid	C3D20R	6.35	17.44
Solid	C3D20R	7.94	27.10
Shell	S4	6.35	17.46
Shell	S4	7.94	27.13
Shell	S4	9.53	38.85
Shell	S8R	6.35	17.45
Shell	S8R	7.94	27.12
Shell	SC8R	6.35	17.45
Shell	SC8R	7.94	27.10

As stated above the solid elements chosen for these models did not include quality aspect ratios. The shear locking phenomenon presented above is clearly seen in the linear solid model results in Table 6. This phenomenon caused the linear solid full integration models to produce overly stiff results and thus poor buckling failure predictions. However, the critical buckling stresses were very similar to the theoretical buckling stresses following the mesh convergence study, seen in Table 7. The one element choice that did not predict the buckling stress well was the C3D8R element.

C3D8T, C3D8RT, and S4T elements were used to predict buckling failure times prior to the mesh convergence study. Additional element types (C3D20T and C3D20RT) were used in a select number of models to understand their effect. Models which include shell elements have a much smaller run time than models with solid elements. The comparison between the two

provides insight into whether or not shell element models can be used in lieu of solid models. Shell elements are known to perform well under bending conditions because bending is included in its fundamental formulation.

Figures 26, 27 and 28 below depict the experimental and predicted (C3D8T, C3D8RT and S4T elements) results of a test with 8mm thick plate, an initial imperfection of 1.5mm and 0.25mm (only for C3D8T elements), an applied stress of 14.61 MPa and an applied heat flux of 38 kW/m². Specifically, Figure 26 depicts the nodal temperature distribution at the center of the plate which does not change with the element type. Figure 27 depicts the out-of-plane deflection results and Figure 28 depicts the in-plane deflection results.

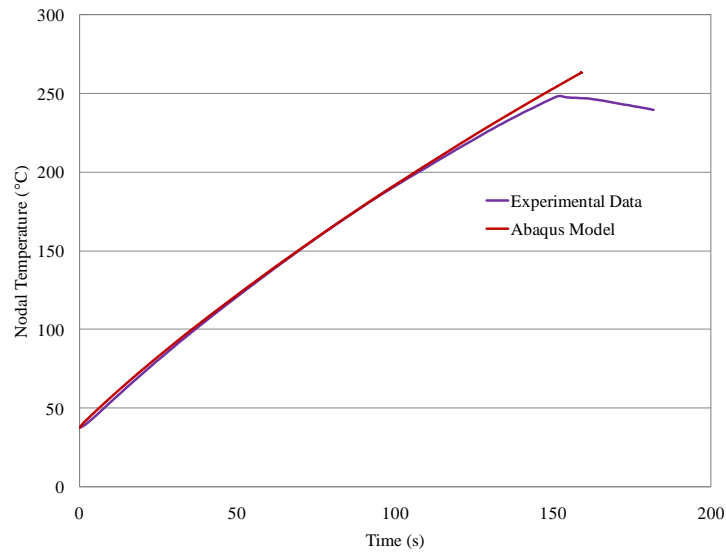


Figure 26. Nodal temperature vs. time at the center of the plate – 38 kW/m² applied heat flux and 14.61 MPa applied stress

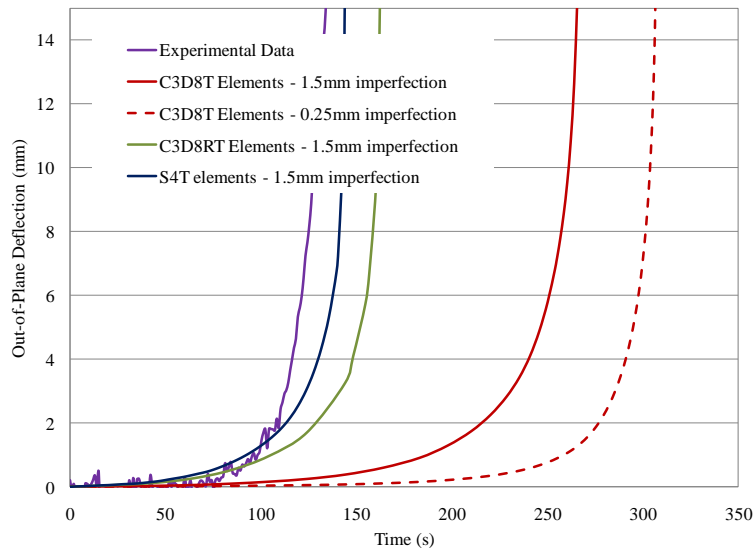


Figure 27. Out-of-plane deflection vs. time at center of plate – 38 kW/m² applied heat flux and 14.61 MPa applied stress

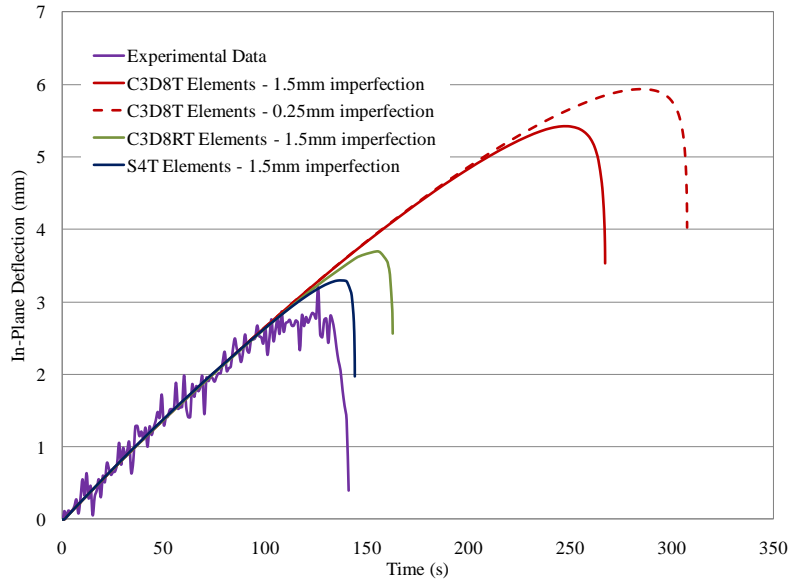


Figure 28. In-plane deflection vs. time at top of plate – 38 kW/m^2 applied heat flux and 14.61 MPa applied stress

The results depicted in Figure 26 reveal that the heat transfer properties (radiation and film condition as well as the heat flux partitioning pattern) provide the model with accurate predictions of temperature. This is apparent in almost all comparisons of the experimental and predicted results. In some cases the heat transfer coefficient or the emissivity may not exactly match experimental conditions and may not give as accurate results as depicted in Figure 26.

The shapes of the out-of-plane and in-plane deflection curves reveal that the compression-controlled failure occurred suddenly around 5-10mm of out-of-plane displacement. Failure times are therefore taken at 10mm of out-of-plane displacement. In this test, the shell models predict failure much closer to the experimental failure than do the linear solid full integration elements. It is apparent that the C3D8T elements experienced shear locking which basically caused the elements to lock onto one another under the compressive applied stress. The C3D8RT elements also show lower times to failures compared to the linear solid full integration elements. This is due to the fact that these elements only have one integration point which caused the stiffness of the model to decrease significantly thus greatly decreasing the effects of shear locking. These elements are not normally suggested for use because under certain conditions (such as bending) these elements can produce extraneous results. One benefit of using C3D8RT elements is that the model run time is significantly lower than the C3D8T elements (0.5 – 1.0 hours as compared to 3-4 hours).

Also, since initial imperfections were not measured experimentally, the range of 0.25mm and 1.5mm was used in the modeling procedure (as stated above). Further investigations into experimental results (on limited samples) reveal that the initial imperfections are nearer towards the 1.5mm value. The curves in Figures 27 and 28 reveal that the initial imperfection does in fact have an effect on failure times. In this particular test, the failure time of the plate with a 0.25mm imperfection is about 50-75 seconds greater than the failure time of the plate with a 1.5mm imperfection.

Predicted times to failure for element types C3D20RT and C3D20T are almost exactly equal. These quadratic solid elements should actually converge to the C3D8RT results if the reduced integration elements are working correctly. This is shown to be true in a 9mm aluminum plate test with 5.19 MPa applied stress and 38 kW/m² applied heat flux. Figure 29 depicts the out-of-plane deflection for each element type with 1.5mm initial imperfection.

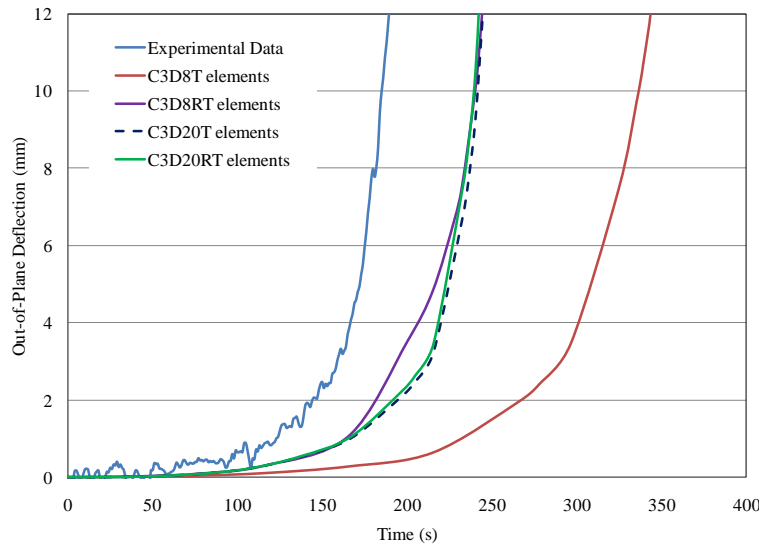


Figure 29. Out-of-plane deflection results – 9mm aluminum plate with 38 kW/m² applied heat flux and 5.19 MPa applied stress

The results for element types C3D20T, C3D20RT and C3D8RT all fall along almost the same exact curve. The C3D8T elements give a poor prediction of the time to failure (100-150 seconds more than the other elements presented). Again, this can be attributed to shear locking. As stated in a previous section, the quadratic solid elements (C3D20T or C3D20RT) are unaffected by shear locking which is made clear in Figure 29.

2.8.2 - Mesh Convergence Study

The results presented above revealed that further investigations into the mesh density as well as the element type was required to produce more accurate predictions of failure. The efficiency or the total run time of the model was also investigated. In engineering applications concerned with finite element analysis, results need to be speedy as well as accurate. It seems from the results presented above, that the solid elements especially needed mesh refinement. Once it is determined that those results are extensively refined and provide more accurate predictions, other element choices (such as shell elements), are implemented and compared to the refined solid element results. This not only will improve the model's efficiency, but also its accuracy.

As stated above, the C3D8T element choice in bending problems may cause problems such as shear locking. This problem can be avoided by considering the element aspect ratio in the models. First a convergence study on the critical buckling load was conducted for the 8mm thick aluminum plate with C3D8 elements to understand how the numerical (FE) results

approach the theoretical results. Five different mesh densities were studied for this type of element; the first with a very coarse mesh and the last with a very fine mesh. Figures 30-32 depict the element size through the thickness for the coarsest mesh, the mesh that was ultimately chosen, and the finest mesh.

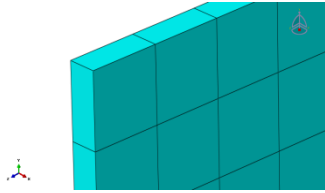


Figure 30. Coarsest mesh –
400 elements

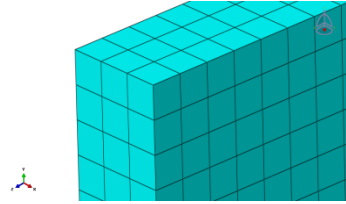


Figure 31. Final mesh –
76,800 elements

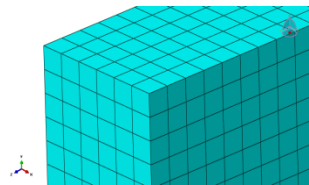


Figure 32. Finest mesh –
614,400 elements

The development of the mesh refinement was simply based on providing a quality element aspect ratio. Figure 30 does not have a high-quality element aspect ratio and only has one element through the thickness. Bending problems require more elements through the thickness to capture the failure mode shape. The buckling model with the mesh from Figure 32 was successfully run. The estimated run time for the coupled temperature-displacement step for the model with the mesh from Figure 32 was over 48 hours, therefore, due to time constraints this model was not run. Figure 31 depicts the final mesh chosen for the 8mm thick aluminum plate models. This same mesh was chosen for 6.35mm thick aluminum plate models due to the fact that the element aspect ratio was not significantly affected. The mesh chosen for the 9.525mm thick aluminum plates included one more element through the thickness with a total of 102,400 elements so as to maintain a quality aspect ratio.

2.8.2.1 – Convergence of Buckling Results

The critical buckling stresses are necessary to converge before running the coupled temperature-displacement step in these models. Figure 33 below shows the C3D8 element buckling stress found at each mesh density (the total number of elements in the model) compared to the theoretical critical buckling stress. Again, as stated above, this convergence study was completed for the 8mm thick aluminum plate. The mesh formulation for the 8mm thick plate was then extended to the 6mm and 9mm thick plates.

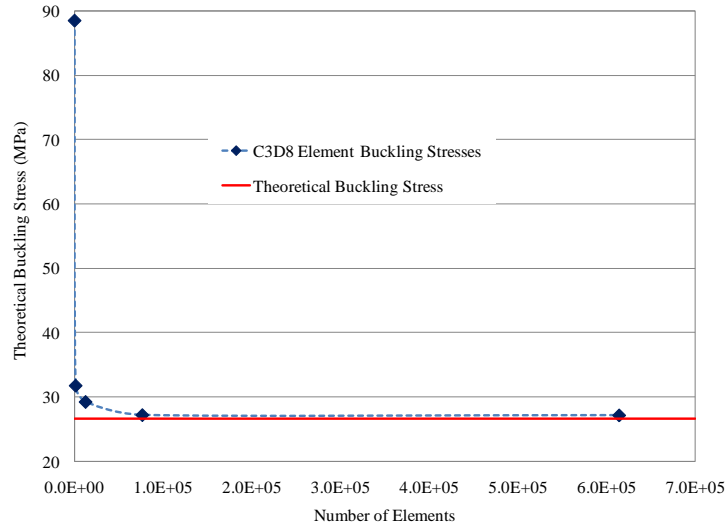


Figure 33. Critical buckling stress vs. number of elements – C3D8 element type

Figure 32 reveals that the first mesh (shown in Figure 30) is not appropriate for this model. The critical buckling stress is about 90 MPa which is significantly different than the theoretical critical buckling stress 26.6 MPa. As the number of elements increased the critical buckling stress began to converge very well to the theoretical critical buckling stress value.

2.8.2.2 - Convergence of Coupled Temperature-Displacement Step

Each of these models with different mesh densities was then run for a particular coupled temperature-displacement test to view the convergence in the out-of-plane and in-plane deflection results. The test chosen to show this convergence is test 25 which has an applied heat flux of 19 kW/m^2 and an applied stress of 14.9 MPa. The out-of-plane deflection results for each of the mesh densities chosen for the C3D8T element type as well as the experimental results are depicted in Figure 34 below.

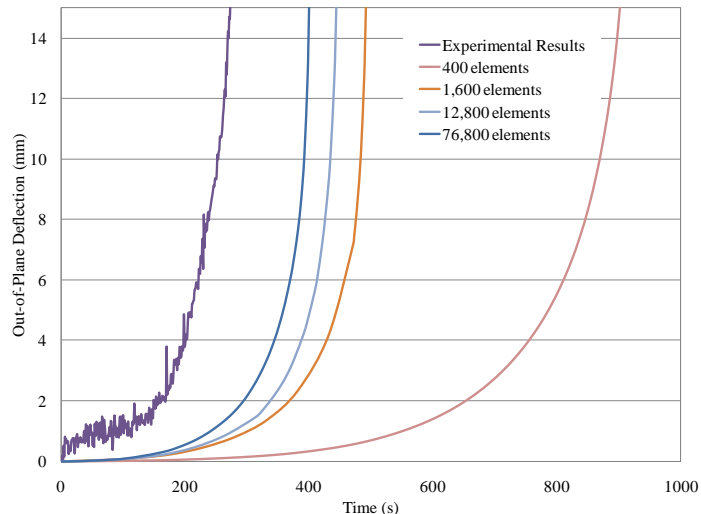


Figure 34. Out-of-plane deflection vs. time curve for C3D8T element type – 19 kW/m^2 heat flux and 14.9 MPa applied stress

As suspected, the model with 400 elements and a poor element aspect ratio did not produce accurate predictions of failure, which is mainly attributed to shear locking. The mesh density shown in Figure 32 (614,400 elements) seemed to be the best choice due to the excellent refinement of the mesh. However, this mesh density was not a feasible choice because of its efficiency; the model was estimated to take about a day and a half or longer to run. Therefore, the mesh density depicted in Figure 31 (76,800 elements) was chosen for the 8mm thick plate C3D8T element models. Without the consideration of the 614,400 element model, the 76,800 element model is shown to have the most accurate out-of-plane deflection predictions shown in Figure 34. It seems though, from the rate of convergence that the 614,400 element mesh probably would not have yielded significantly better results; at the most 10-20 seconds of a time to failure difference. As stated previously, the 6.35mm thick plate will also use 76,800 elements with 3 elements through the thickness (same as 7.938mm thick plate) and the 9.525mm thick plate will use 102,400 elements with 4 elements through the thickness.

2.8.2.3 – Effect of Shell Element Type

The shell element models also showed convergence when the mesh density was changed. Originally, three integration points through the shell thickness was used in the shell models. Keeping this parameter constant, the number of elements along the width and the length were varied. The critical buckling loads for each of the meshes chosen were basically unaffected by the choice of mesh density and were all very close to the theoretical buckling loads. After the shell mesh density reached about 6,400 elements (across the width and the length of the plate) the results converged and there were no differences. This can be seen in the results of test 25 (applied heat flux of 19 kW/m², an applied stress of 14.9 MPa, and an initial imperfection of 1.5mm) below in Figure 35.

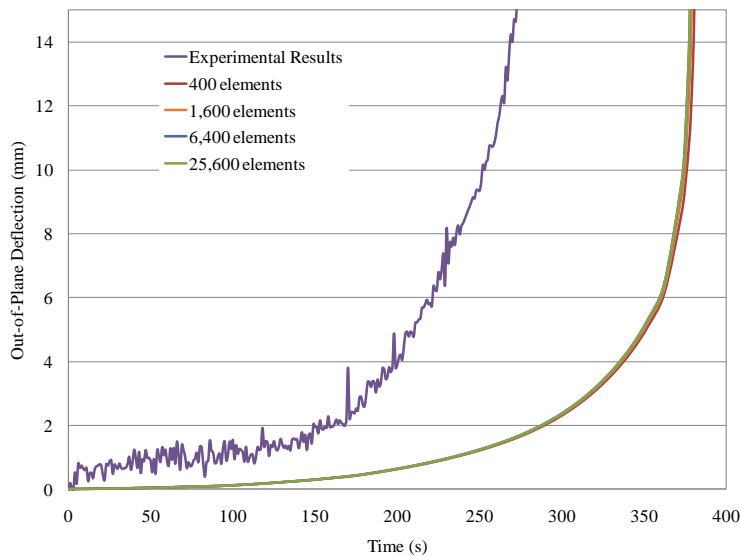


Figure 35: Out-of-plane deflection vs. time curve for S4T element type – 19 kW/m² heat flux and 14.9 MPa applied stress

The number of integration points through the thickness of the S4T element model was increased to see its effect. As seen in Figure 36, the shell models with 3, 5, and 7 integration points showed convergence. The 5 and 7 integration point shell models are almost exactly the same therefore shell models with 5 integration points was used for the final results. The out-of-plane deflection results can be seen in Figure 36 with an applied heat flux of 8 kW/m^2 , an applied stress of 19.43 MPa , and an initial imperfection of 1.5 mm .

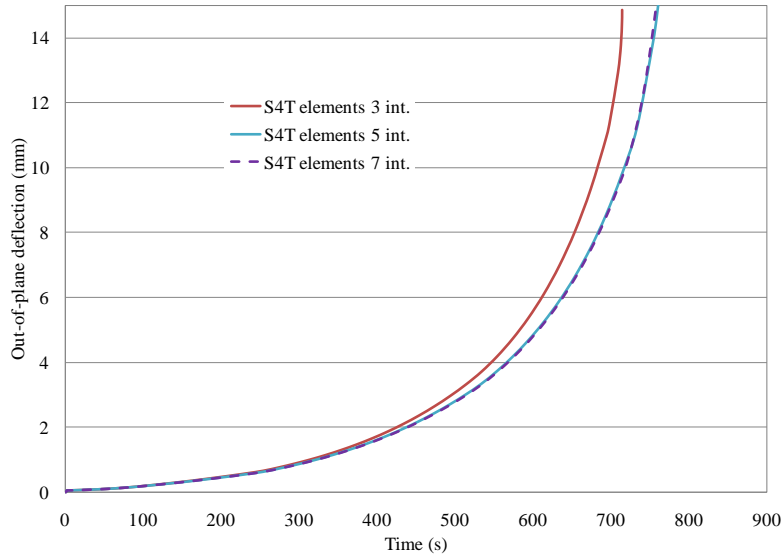


Figure 36. Out-of-plane deflection vs. time curve for S4T element type – 8 kW/m^2 heat flux and 19.43 MPa applied stress

Other shell elements were also investigated (S8RT and SC8RT). Shown in Figure 37, the S8RT element results provide slightly closer predictions to the solid element results. The SC8RT element results also match very well to the solid element results. The S4T and SC8RT models take the least amount of time to run; about 20 minutes. However, the SC8RT models for certain tests may take longer because a fixed and smaller time increment is required to successfully run the model. The S8RT element models take about 45 to 60 minutes to run. Ultimately, the S4T model results were used in the final results section of this thesis.

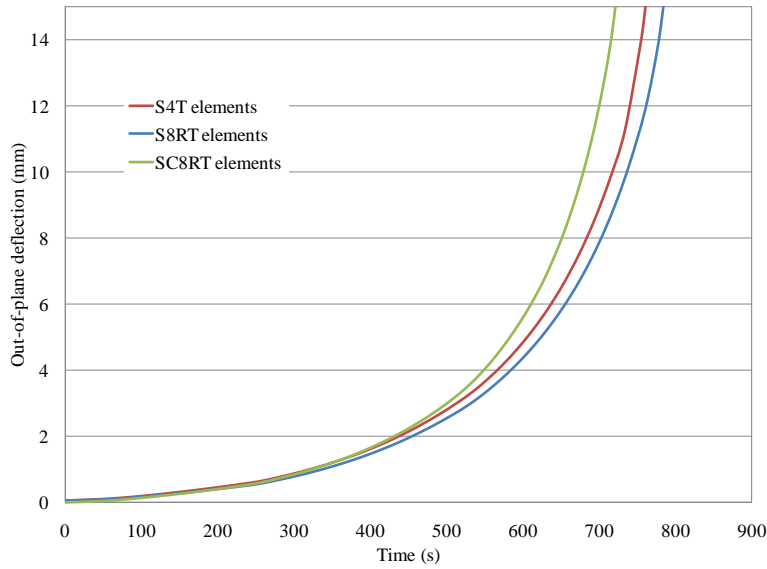


Figure 37: Out-of-plane deflection vs. time curve – comparison between shell element types (S4T, S8RT, and SC8RT)

2.8.2.4 – Effect of Solid Element Type

As discussed in a previous section the C3D20T and C3D8T elements should show very similar results if the C3D8T elements are not experiencing shear locking. Shear locking does not occur when C3D20T elements are used. Figure 38 below depicts the out-of-plane deflection results for a test with a 6mm thick plate, 38 kW/m^2 applied heat flux and a 4.05 MPa (20% of the buckling load) applied stress. The C3D8T and the C3D20T results are plotted along with the experimental results.

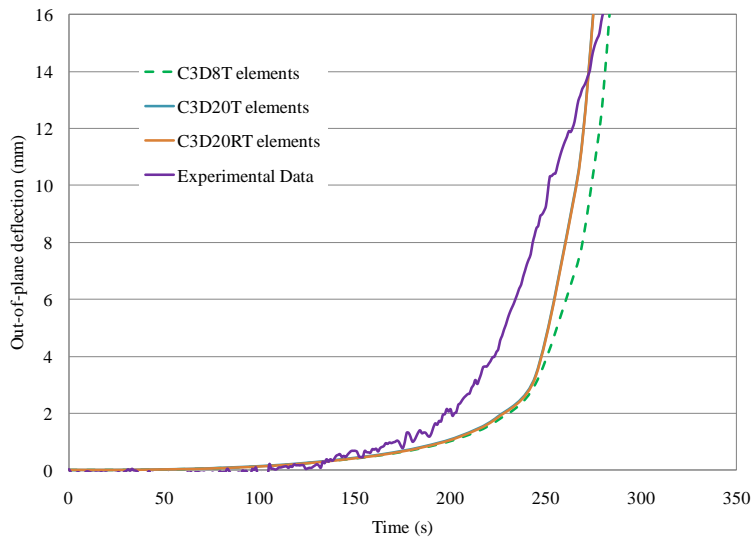


Figure 38. Out-of-plane deflection vs. time curve – comparison between C3D8T and C3D20T elements

The results above show that for this particular model, the C3D8T elements are not experiencing shear locking. However, for other models the C3D8T element results do not converge to the C3D20T element results like the above graph depicts. Results are shown and discussed in the section below.

Prior to the presented mesh convergence study, the C3D8RT elements predicted failure closer to the experimental times than the C3D8T elements. The success seen in these elements were due to the number of elements through the thickness of those models. Because of this the C3D8T element models were overly stiff and using reduced integration elements decreased the stiffness significantly thus allowing for earlier predictions of failure. However, following the mesh convergence study, the C3D8RT elements did not behave as before. The *buckle step for an 8mm thick plate using C3D8RT elements produced a critical buckling stress of about 24 MPa as opposed to 27 MPa. This model, however, used the default hourglass control setting as opposed to the enhanced hourglass control setting. The enhanced hourglass control setting is implemented to the input file as follows:

***Solid Section, elset=_PickedSet77, controls=EC-1, material="Aluminum 5083"**

This is the solid section definition line (which is input before the end of the part definition) and the controls keyword is set equal to the name of the control which is defined after the assembly definition as seen below:

***Section Controls, name=EC-1, hourglass=ENHANCED
1., 1., 1.**

The three numbers are the dimensionless hourglass control scaling factors used for each displacement degree of freedom in the model. The default factors for the enhanced hourglass control keyword are 1, 1, and 1. These may be changed as necessary.

After the implementation of the enhanced hourglass control keyword in the input file, the critical buckling stress increased from 24 MPa to about 27 MPa. The *coupled temperature-displacement step was then ran for test 55 (with 1.5mm initial imperfection) to see how the out-of-plane deflections compared for both the C3D8RT (default hourglass control) and the C3D8RT (enhanced hourglass control) element types. This comparison is depicted in Figure 39 below.

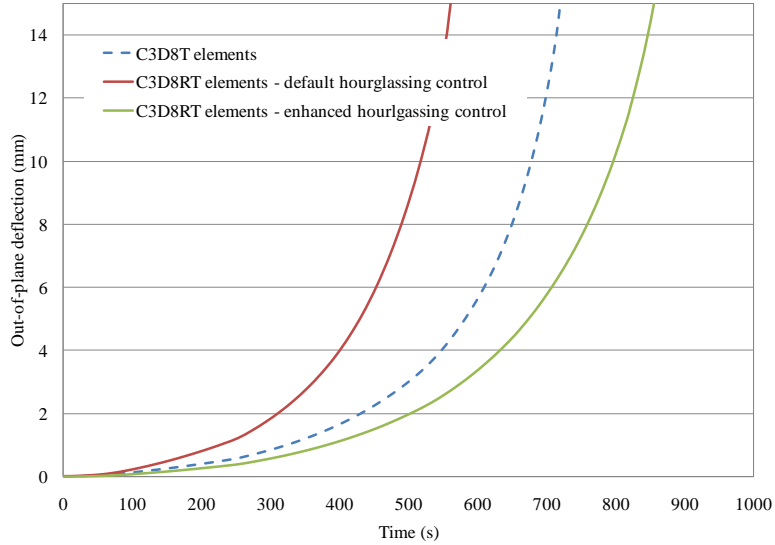


Figure 39. Out-of-plane deflection vs. time curve – comparison between reduced integration hourglass controls

The enhanced hourglass control reduced integration elements produce slightly closer results to the full integration elements than do the default reduced integration elements. However, these elements must be used with caution because this significant difference is entirely due to the addition of artificial strain energy into the models. Figure 40 below shows the total artificial strain energy in the test 55 model for C3D8T, C3D8RT default hourglass control, and C3D8RT enhanced hourglass control element types.

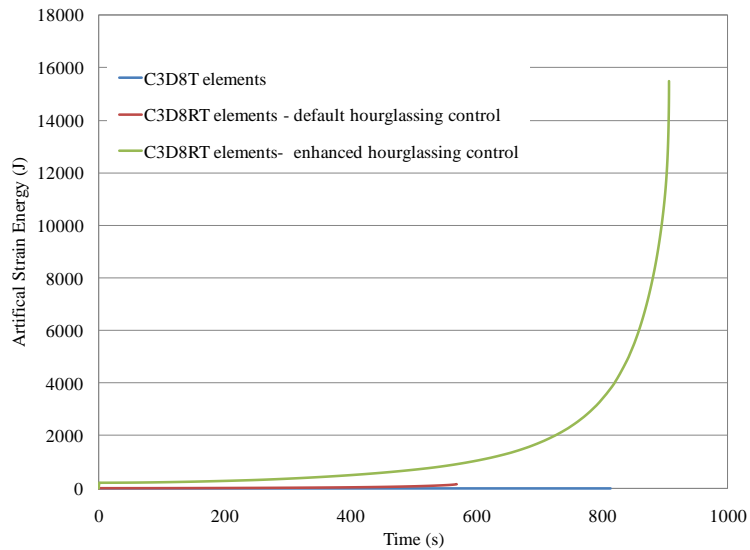


Figure 40. Artificial Strain Energy (kJ) vs. time (s) curve

The C3D8T elements have zero artificial strain energy while the C3D8RT default hourglass control and the C3D8RT enhanced hourglass control have a maximum of 144 kJ and 15504 kJ respectively.

2.8.2.5 – Comparison of Solid and Shell Element Types

For the majority of the coupled temperature-displacement tests, shell and solid models do in fact produce very similar results. The out-of-plane deflections for three tests are shown in Figures 41, 42, and 43. These tests all have different heat fluxes and various applied loadings (less than 70% of the buckling load). Figure 41 depicts the out-of-plane deflection curve for a 8mm thick plate which has an applied heat flux of 8 kW/m² and an applied stress of 19.43 MPa (70% of the buckling load of an 8mm thick plate).

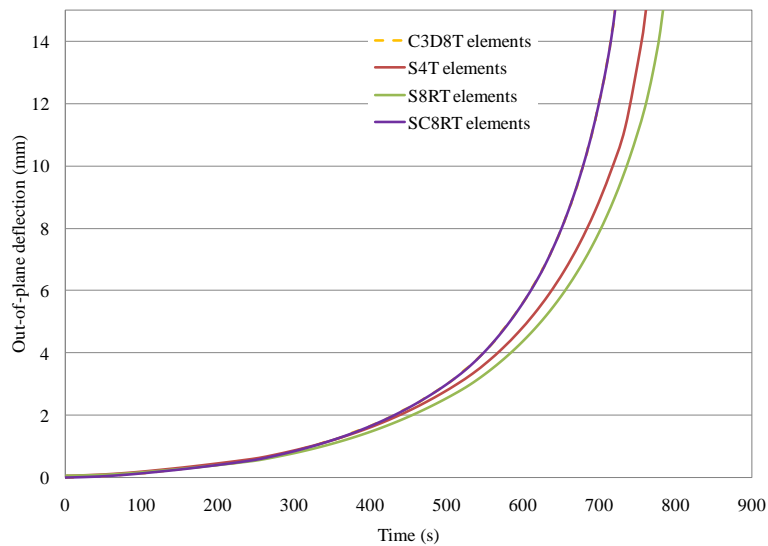


Figure 41. Out-of-Plane Deflection vs. Time Curve – 8mm thick plate with an applied heat flux of 8 kW/m² and applied stress of 19.43 MPa

Figure 42 depicts the out-of-plane deflection curve for a 6mm thick plate which has an applied heat flux of 38 kW/m² and an applied stress of 4.05 MPa (20% of the buckling load of a 6mm thick plate). In addition this model includes a 1.5mm initial imperfection. The C3D8T results are plotted in Figure 42 along with the S4T and S8RT element results. The results for the C3D8T elements and the SC8RT elements match exactly. The S4T and S8RT elements also match well with the solid and continuum shell elements (within 40 seconds). This test amongst other 6mm thick plate tests reveals that the mesh created for the 8mm thick plate could in fact be extended well to the 6mm thick plate.

Finally, Figure 43 depicts the out-of-plane deflection curve for an 8mm thick plate which has an applied heat flux of 38 kW/m² and an applied stress of 3.39 MPa (10% of the buckling load of an 8mm thick plate). Each of these models also includes a 1.5mm initial imperfection. Along with the experimental data, the S4T and S8RT element results are plotted in Figure 42.

Similarly to the results depicted in Figure 42, the results for both the solid and shell models in Figure 43 match very well.

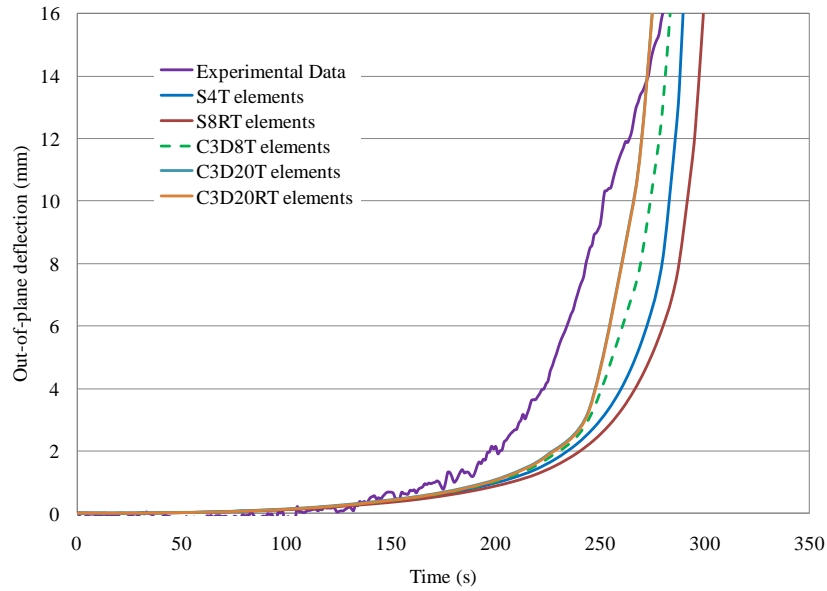


Figure 42. Out-of-Plane Deflection vs. Time Curve – 6mm thick plate with an applied heat flux of 38 kW/m² and applied stress of 4.05 MPa

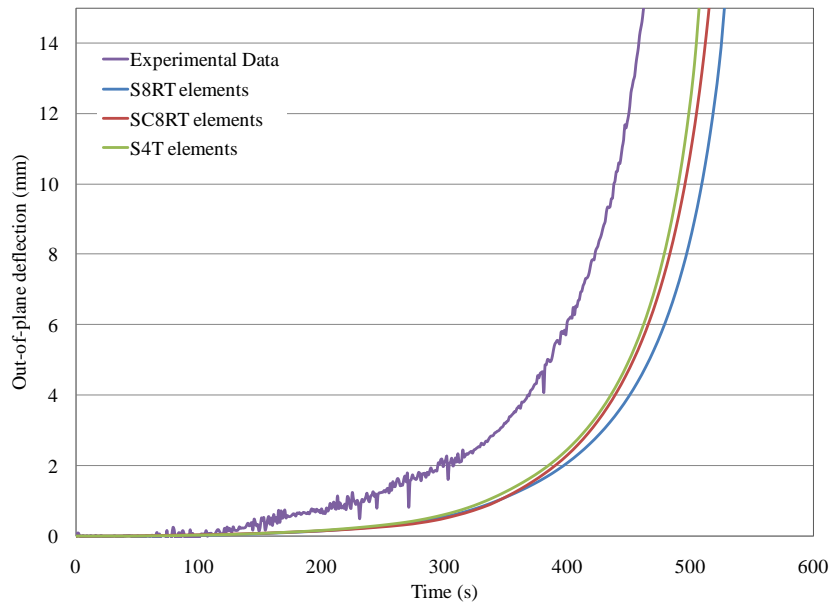


Figure 43. Out-of-Plane Deflection vs. Time Curve – 8mm thick plate with an applied heat flux of 38 kW/m² and applied stress of 3.39 MPa

The solid and shell models may not always produce results that match well to each other. Figure 44 below depicts a test with a 6mm thick plate, a low heat flux (8 kW/m²) and a very large applied stress (80% of the buckling stress). The S4T, S8RT, C3D20T, and C3D20RT

elements all produce very similar predictions of failure. However, the C3D8T elements predict slightly longer times to failure. This suggests that the affects of shear locking is more significant when the models are subjected to high applied stresses (greater than 80% of the critical buckling stress).

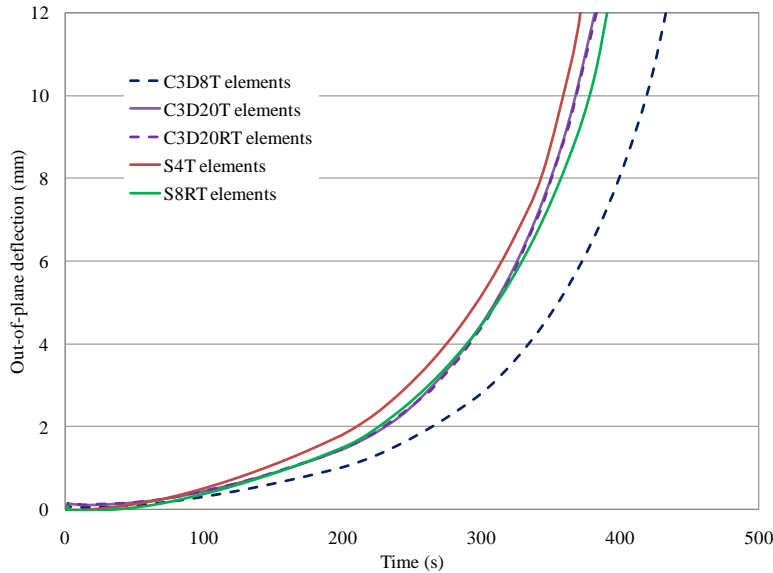


Figure 44. Out-of-Plane Deflection vs. Time Curve – 6mm thick plate with an applied heat flux of 8 kW/m² and applied stress of 14.61 MPa

The results presented in this section lead to the conclusion that fully integrated linear solid elements may not be appropriate for this type of analysis even upon mesh refinement. Also, the quadratic solid elements (both full and reduced integration) consistently produce very similar results to the shell element models thus proving that the shear locking phenomenon is only relevant to the C3D8T element type. The results presented above reveal S4T elements are the most efficient and accurate element type to use in the aluminum buckling simulations presented in this thesis. These conclusions can be extended to more complicated aluminum structures which can include plates and stiffeners of the same type presented in this thesis.

2.9 - Final Results

Experimentally, about 40 different tests were successfully run. S4T elements were used to model each of these tests. Other shell and solid element types were used for selected tests as seen in above sections. Times to failures were determined for both the experimental results and predicted results and then were plotted on a log-log scale graph to produce an overall picture of the influence of each test parameter (thickness, applied heat flux, and applied stress).

2.9.1 – Shell Elements Final Results

2.9.1.1 – Importance of Creep in Compression-Controlled Failure

Creep is extremely important in the compression-controlled failure of the aluminum plates. In Figure 45 below, the out-of-plane deflection vs. time curves are depicted for one particular test. Specifically the experimental results, the model results with creep, and the model results without creep are depicted for a test with 7.19 MPa applied stress, 38 kW/m² applied heat flux, and a thickness of 8mm.

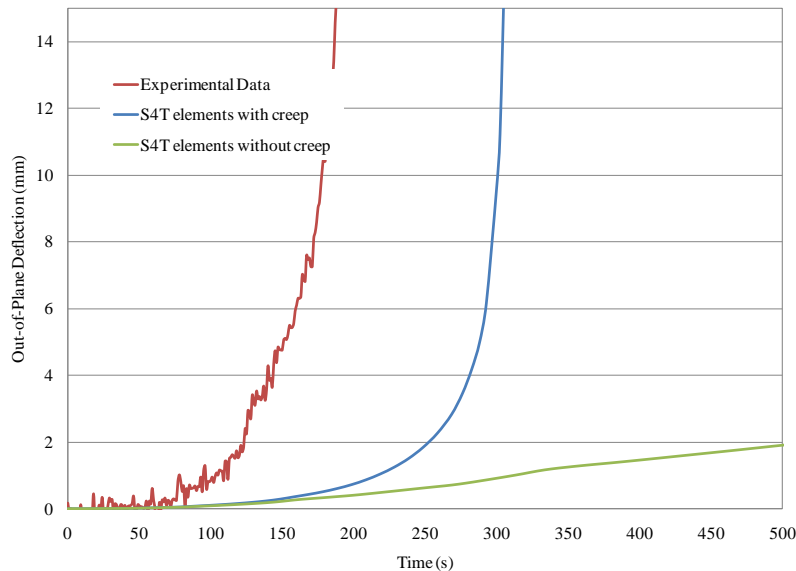


Figure 45. Out-of-Plane Deflection vs. Time – applied stress of 7.19 MPa and applied heat flux of 38 kW/m²

The results depicted in Figure 45 reveal that creep is in fact important in these analyses. Without the inclusion of creep in the finite element models, the shape of the out-of-plane deflection curve does not at all reflect the experimental data or the model which includes creep. Also, the out-of-plane deflection for the model without creep seems to plateau around 2mm and then past the 500 seconds depicted in the graph, the deformation increases quite slowly until failure occurs well past the experimental time to failure.

2.9.1.2 – Abaqus Power Law Creep Results

S4T elements were chosen to produce the final shell results. As stated before, overall this element type produced both accurate and very efficient results. Figure 46 below depicts the experimental vs. predicted times to failure for the S4T element type with a 1.5mm initial imperfection. The Abaqus power law creep is utilized in the results presented in Figure 47.

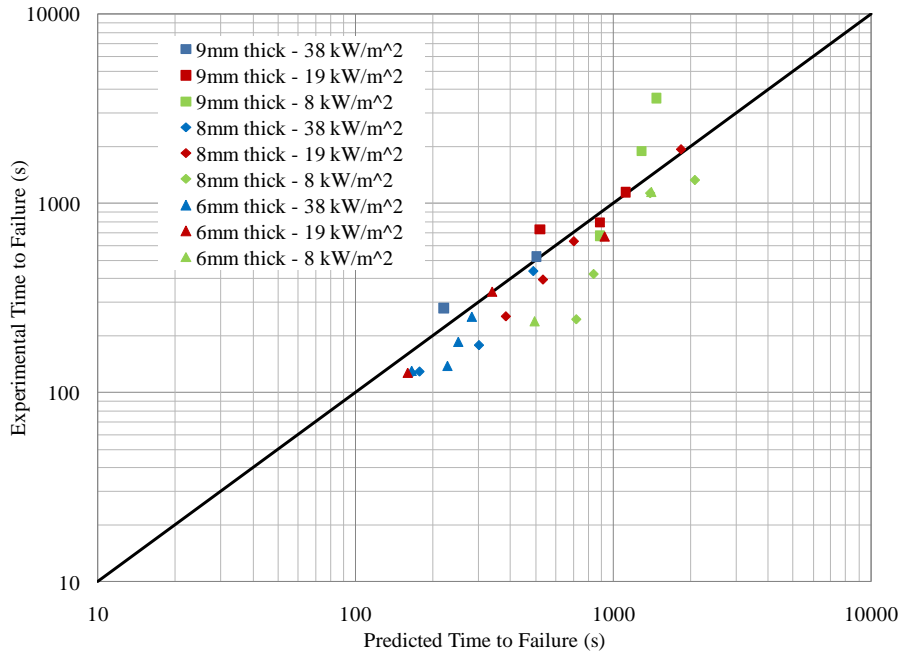


Figure 46. Experimental vs. Predicted Times to Failure – S4T elements with the Abaqus power law creep model

It is apparent in the results depicted in Figure 46 that under these certain conditions, the predicted times to failure match very closely to the experimental times to failure. If a 0.25mm initial imperfection was used for all of these tests the results would shift to the right by 50-75 seconds. This shift is still small enough to produce reasonable predictions of failure.

2.9.1.3 Dorn-Hamathy Creep Law Results

Figure 47 below depicts the experimental vs. predicted times to failure of S4T elements which utilized the Dorn-Harmathy creep law model. Again, a 1.5mm initial imperfection was used in these models.

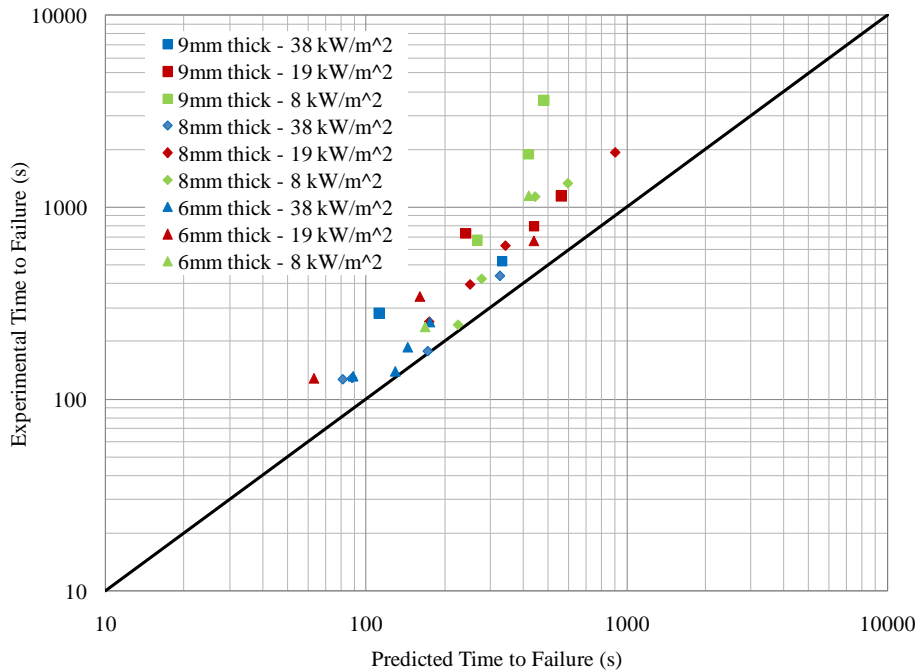


Figure 47. Experimental vs. Predicted Times to Failure – S4T elements with the Dorn-Harmathy creep law

The results depicted in Figure 47 reveal that the predicted times to failure for the Dorn-Harmathy creep law models are consistently lower than the experimental times to failure, with a few exceptions. The blue points on the graph symbolize models with an applied heat flux of 38 kW/m² which provide much closer time to failure predictions to the experimental results than the other models.

Finally, the both creep models are compared to each other in Figure 48. This reveals that the predicted times to failure for the Dorn-Harmathy creep law models are consistently less than the Abaqus power law creep models. These differences were investigated at an analytical level and creep strain versus time curves (Figures 49 and 50) were produced for both creep models to understand the differences between the two.

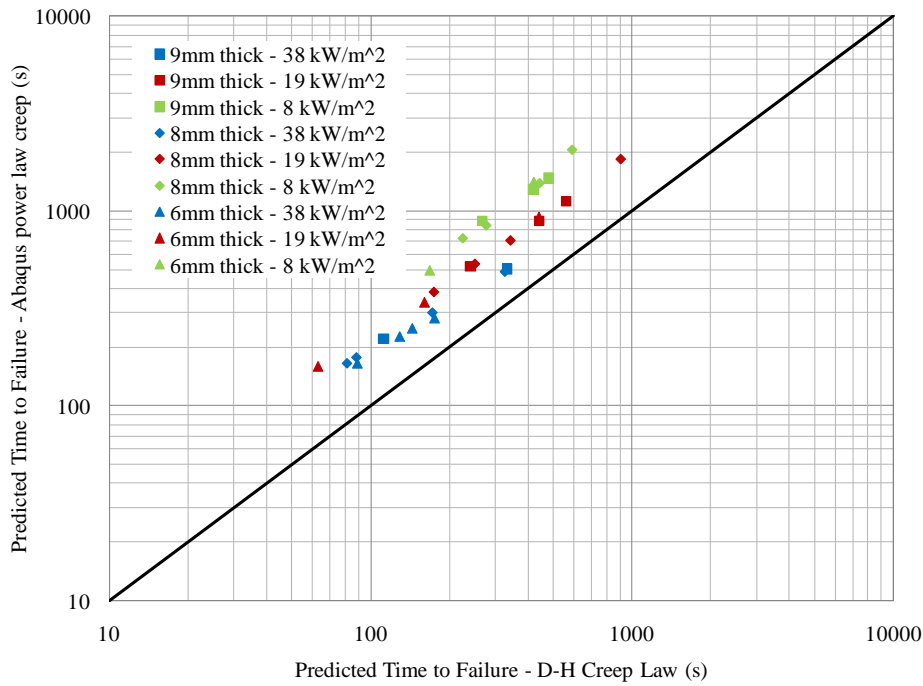


Figure 48. Predicted times to failure for the Abaqus power law creep vs. the Dorn-Harmathy creep law models – S4T elements

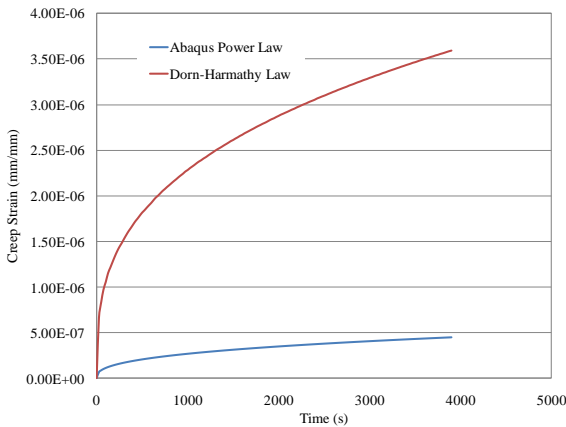


Figure 49. Creep Strain vs. Time - 50°C
4MPa applied stress

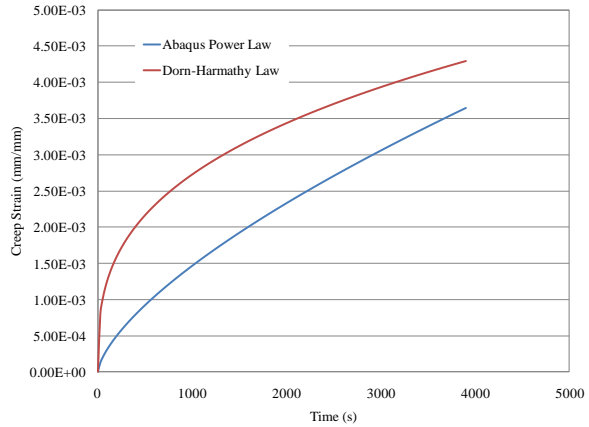


Figure 50. Creep Strain vs. Time – 300°C
10MPa applied stress

Figure 48 indicates that the differences between each creep model are less when the applied heat flux is high. The analytical results depicted in Figures 49 and 50 reveal that the Dorn-Harmathy creep law models consistently produce greater creep strains than the Abaqus power law creep models. Figures 49 and 50 also reveal the same conclusion drawn from Figure 48; as the failure temperature (due to a high heat flux) is greater the differences between the creep models become significantly smaller.

2.9.2 – Effect of Emissivity on Plate Surface Temperature

Experimentally, the aluminum plates were painted black on the heat exposed surface and left unpainted on the back surface. A select few tests were run with a different emissivity on the front and back surface: unpainted on both surfaces, painted black on both surfaces, unpainted on the front surface and painted on the back surface.

On the modeling end of this, because the heat flux gages were painted black along with the front surface of the majority of the tests, the applied heat flux has to be adjusted within the model for the select few tests which have the front surface unpainted. Equations 18 and 19 below describe the governing equations for the heat flux of the surface and the heat flux of a heat flux gage respectively.

$$q_s'' = \varepsilon_s q_{RAD}'' - \varepsilon_s \sigma T_s^4 + h(T_g - T_s) \quad \text{Equation 18}$$

$$q_{hfg}'' = \varepsilon_{hfg} q_{RAD}'' - \varepsilon_{hfg} \sigma T_{hfg}^4 + h(T_g - T_{hfg}) \quad \text{Equation 19}$$

Solving for q_{RAD}'' in Equation 19 results in Equation 20 below,

$$q_{RAD}'' = \frac{1}{\varepsilon_{hfg}} [q_{hfg}'' + \varepsilon_{hfg} \sigma T_{hfg}^4 + h(T_g - T_{hfg})] \quad \text{Equation 20}$$

The result from Equation 20 is then plugged into Equation 18. After some algebraic manipulations Equation 21 describes the heat flux of the surface when the emissivity of the surface is equal to the emissivity of the heat flux gage. Equation 22 describes the heat flux of the surface when the emissivity of the surface is not equal to the emissivity of the heat flux gage.

$$q_s'' = q_{hfg}'' - \varepsilon_s \sigma (T_{hfg}^4 - T_s^4) + h(T_{hfg} - T_s) \quad \text{Equation 21}$$

$$q_s'' = \frac{\varepsilon_s}{\varepsilon_{hfg}} q_{hfg}'' - \varepsilon_s \sigma (T_{hfg}^4 - T_s^4) + h(T_{hfg} - T_s) \quad \text{Equation 22}$$

If the exposed surface has an emissivity of 0.2 (unpainted) the applied heat flux values on the front surface of the plate needs to be multiplied by the ratio of $\frac{0.2}{0.95} = 0.211$ in order to obtain accurate temperature distributions.

Figure 51 below depicts the nodal temperature results of a series of heat transfer tests all with an applied heat flux of 19 kW/m^2 and different surface conditions.

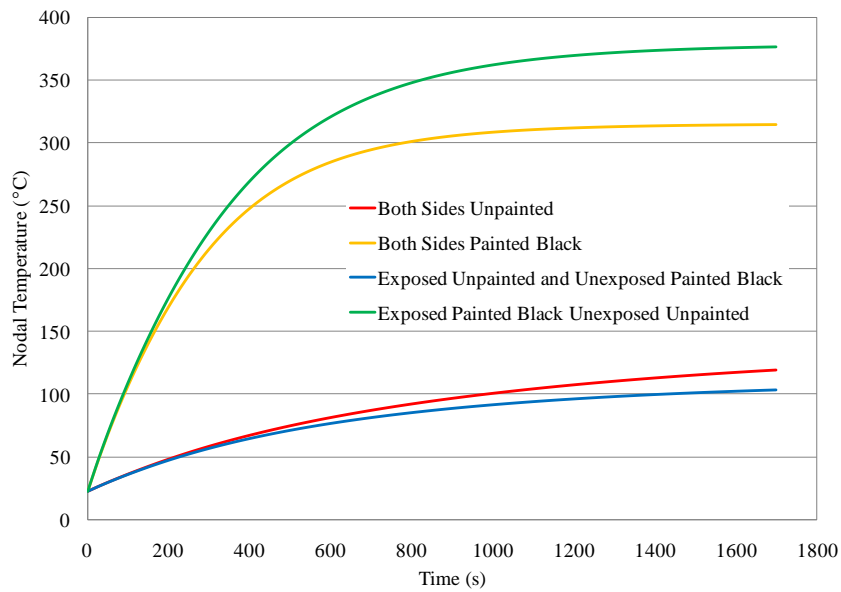


Figure 51. Effects of Emissivity on exposed and unexposed surfaces
 Nodal Temperature vs. Time – 19 kW/m^2 applied heat flux

As suspected the maximum temperature at the center of the plate is achieved when the exposed side is painted black and the unexposed is unpainted. The scenario in which the minimum temperature is achieved is when the exposed side is unpainted and the unexposed side is painted black.

2.9.3 - Effect of Insulation on the Exposed Surface

Experimentally, for five different testing scenarios, insulation (Superwool 607) was attached to the exposed surface of the aluminum specimen, with either aluminum caps/pins or stainless steel wire. Each test had the same applied heat flux, 38 kW/m^2 , the same thickness, 8mm, and different applied mechanical stresses, ranging from 50-75% of the critical buckling stress.

The models created in Abaqus to simulate these tests utilized shell elements (S4T). The “composite layup” option in Abaqus was used to simulate the two different materials, Aluminum and Insulation. In this composite layup option the thickness as well as the number of integration points through the thickness was required input for the two materials. A thickness of 8mm and 12.7mm was used for the aluminum plate and the insulation respectively. The number of integration points through the thickness for both materials was 5.

Figure 52 below, depicts the nodal temperature vs. time curves at the center of the exposed insulation, the interface of the aluminum and the insulation, as well as the unexposed side of the aluminum for one particular test. Experimentally, thermocouples were only attached on the unexposed side of the aluminum plate. The experimental results shown in Figure 52 are taken from the center of the unexposed side of the specimen. The initial temperature for this particular test was about 27°C . Also, the emissivity of the exposed surface was 0.4 due to the insulation and as explained in section 2.9.2, the experimentally applied heat flux values used in the finite element models had to be multiplied by the fraction $\frac{0.4}{0.95}$, which equals 0.38. Also, the initial imperfections in the experiments were measured for these test specimens and are input into the finite element models.

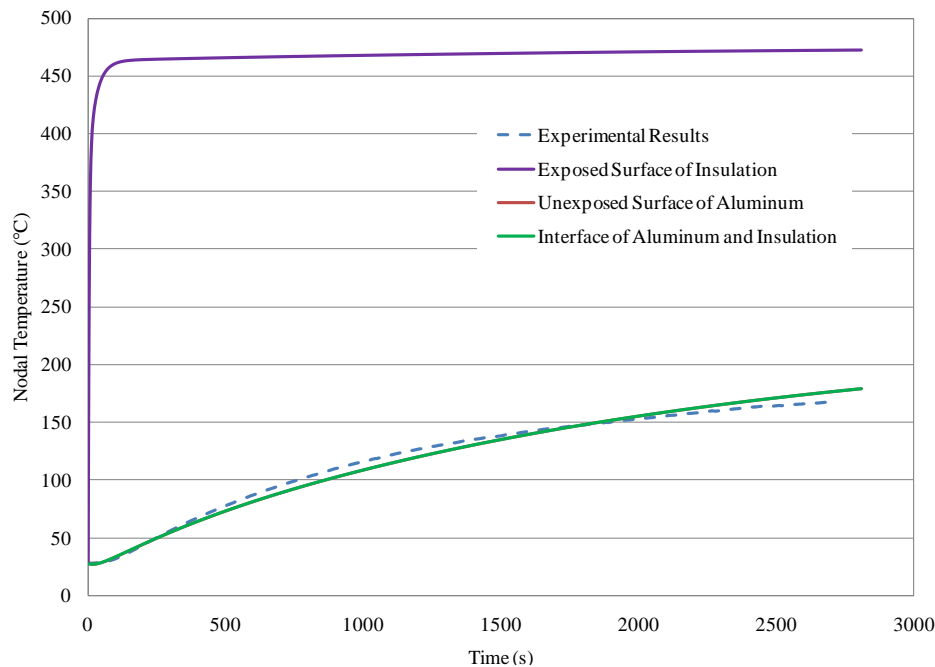


Figure 52. Nodal Temperature vs. Time with insulation on the exposed surface – 38 kW/m^2 applied heat flux

The results depicted in Figure 52 reveal that the experimental thermal conditions for this particular test match very closely to the predicted results. What is not seen so clearly in Figure 52 is that the temperature vs. time for the interface of the aluminum and insulation exactly matches the temperature vs. time of the unexposed side of the aluminum. Also, the temperature experienced in the insulation is extremely high but the insulation is preventing a large conduction of the heat through the aluminum. Typically, for the aluminum plates without insulation, an applied heat flux causes temperatures of about 250°C at around 150 seconds of exposure time (Figure 26). In the tests with insulation, seen in Figure 52, the temperature of the aluminum after 150 seconds of exposure time was only about 40°C.

Figures 53 and 54 below depict an out-of-plane deflection vs. time curve and an in-plane deflection vs. time curve respectively for the same test as seen in Figure 52. The mechanical applied stress for this particular test was about 60% of the critical buckling load; 16.3 MPa. The initial imperfection measured experimentally was about 1.7mm.

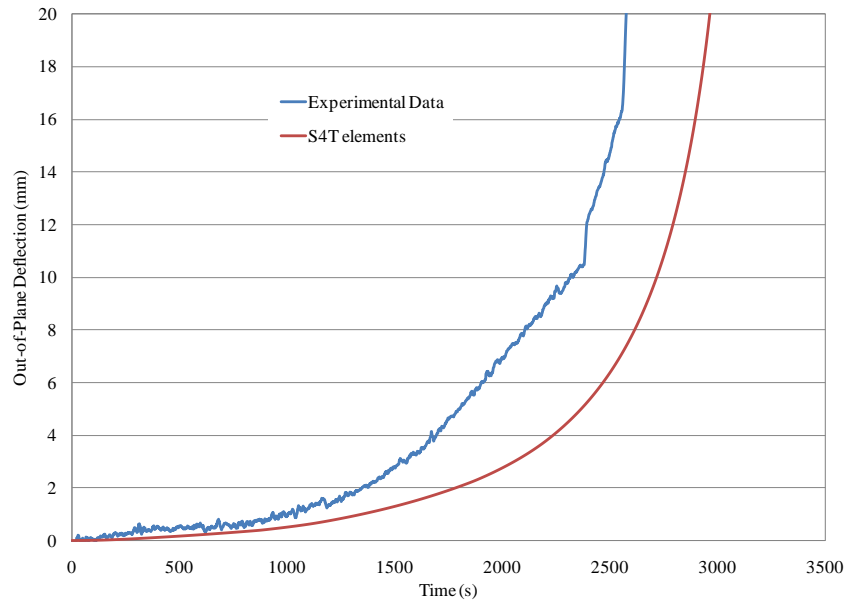


Figure 53. Out-of-Plane Deflection vs. Time with insulation on the exposed surface – 38 kW/m² applied heat flux and 16.3 MPa applied stress

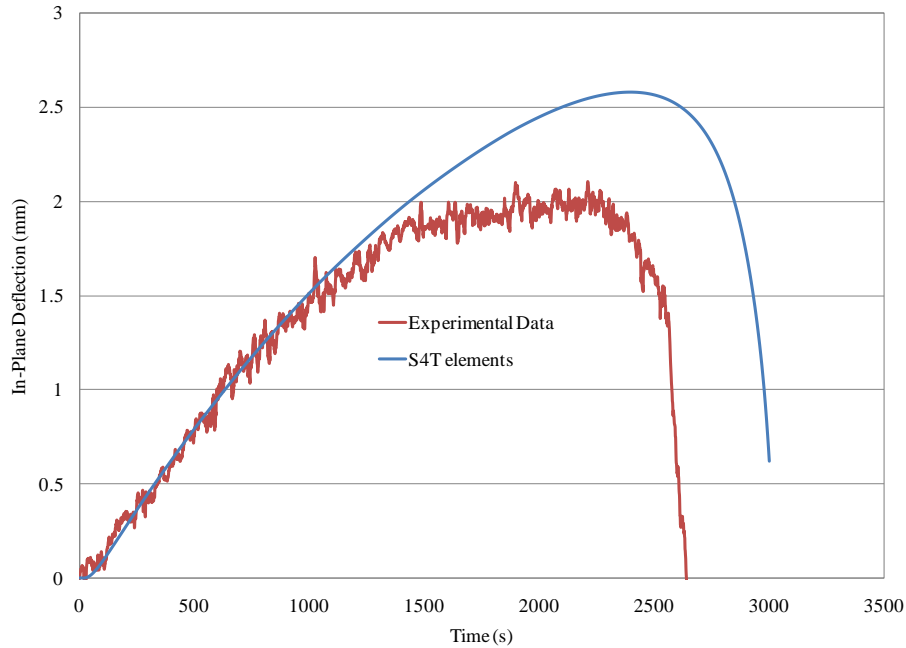


Figure 54. In-Plane Deflection vs. Time with insulation on the exposed surface – 38 kW/m^2 applied heat flux and 16.3 MPa applied stress

The experimental time to failure for the test depicted in Figures 52-54, is about 2300 seconds while the predicted time to failure is about 2700 seconds. Overall, the difference in time to failure is about 400 seconds. As shown in previous sections, the out-of-plane and in-plane deflection results are sensitive to the initial imperfection. However, even when the initial imperfection value is known experimentally and used in the finite element model, the results still differ significantly (depicted in Figures 53 and 54). This leads to the conclusion that there is another parameter involved in these tests that has more of an influence in the mechanical results than the initial imperfection. The section which describes the comparison between creep models reveals that the results are very sensitive to the choice of creep curve fitting law. This parameter is definitely the one in this study which has the most variability and could cause these significant differences in the mechanical results.

2.10 – Discussion of Results

The effects of several different parameters on the prediction of compression-controlled failure of aluminum plates through the use of finite element modeling were studied in this thesis. In general, these parameters consist of the applied heat flux, the applied compression stress, the plate thickness, the mesh density, the initial imperfection, the element type, the emissivity of the exposed surface, and the creep curve-fitting model. The results from these parameter studies were then validated with experimental data.

In the finite element models partitioning was utilized to map the 8, 19, and 38 kW/m² applied heat flux values. This method provided accurate agreement between predicted and experimental temperature distributions on the surfaces of the aluminum plate. The applied stress was also varied according to the critical buckling load of the three plate thicknesses (10% - 80% values). Numerous experimental results of tests with varying applied stresses, applied heat fluxes, and plate thicknesses allowed for a wide range of data for finite element model validation.

Investigations into the mesh density of the finite element models revealed a significant dependence for certain element types as well as certain testing conditions. Specifically, the full integration linear solid element types produced results which varied significantly as the mesh density changed. This is mainly due to the shear locking phenomenon. The use of these types of elements also revealed their dependence on the element aspect ratio. The reduced integration linear solid elements also ran into problems due to hourglassing. The shell elements did not show a significant dependence on the mesh density and did not run into problems with hourglassing or shear locking.

The initial imperfection of the aluminum plate caused results to vary significantly. Experimentally, the initial imperfection was not measured and the range of 0.25mm to 1.5mm initial imperfection was used in the models. The difference in the time to failures of the lower and higher range of initial imperfection was about 50-75 seconds.

Two types of creep data fitting procedures were also implemented into the finite element models. The Abaqus time-hardening power law creep model as well as the Dorn-Harmathy creep model was used to study how the choice of creep model affected the coupled temperature-displacement step results. The results showed that the choice of creep model had an extremely significant effect on the results. The times to failure for the models which utilized the Dorn-Harmathy creep law were consistently lower than the models which utilized the Abaqus power law creep approach. The analytical results (or the one element model results) revealed that this is because the Dorn-Harmathy creep law produced consistently larger creep strains than the Abaqus power law creep approach. However, these differences are much less significant at higher temperatures.

In general, the results reveal that predicting the compression-controlled failure of the aluminum plates is possible with finite element analysis. However, large variability is experienced with certain parameters, specifically within the constitutive model.

Chapter 3 – Conclusions & Future Work

One of the main conclusions to draw from this study is that variability is associated with finite element analysis. Specifically, in the analyses presented in this thesis, the variability lies mainly within the constitutive laws. Refinement of the constitutive laws is necessary for more accurate predictions.

Creep is the constitutive property with the most variability. Experimentally, creep tests are performed at high temperatures and high applied stresses in order to quickly obtain raw creep data. The applied stresses and temperatures of the tests presented in this thesis are not within the range of the experimental creep data. In order to include creep in the finite element models, curve-fitting of the available data must be utilized. This can cause problems because this makes the assumption that similar creep mechanisms are occurring at lower temperatures/stresses as higher temperatures/stresses. This could possibly be a correct assumption but is unknown until experimental creep tests are completed at lower temperatures and stresses. If at all possible, experimental creep tests should also be repeated to understand the variability within the samples.

At a material level, not only could material properties vary within the same batch but they could also have variability depending on which manufacturer they were produced from. This problem could be somewhat avoided by first understanding the range of variability and presenting the results as a range of possible outcomes. Specifically, for creep properties, the microstructure of the aluminum could be viewed at different temperatures which could lead to an understanding of what types of creep mechanisms are present. As a result, raw creep data could be curve-fitted for certain temperature ranges with differing parameters in each range providing a more accurate constitutive creep law for the finite element models.

However, overall, the finite element models presented in this thesis provide accurate predictions of failure. In the future, the results presented in this thesis can provide a framework for more complicated aluminum structures.

List of Resources

- [1] Sielski, R. A., 2007, "Review of Structural Design of Aluminum Ships and Craft."
- [2] Muckle, W., 1964, "The Development of The Use of Aluminium in Ships," Transactions of the North-East Coast Institution of Engineers and Shipbuilders, 80(6), pp. 219-238.
- [3] Taylor, P., and Sielski, R. A., 2008, "Research needs in aluminum structure," Ships and Offshore Structures, 3(1), pp. 57-65.
- [4] Maljaars, J., 2006, "Fatigue of aluminium bridge decks," Structural engineering internation; journal of the International Association for Bridge and Structural Engineering (IABSE), 16(4), pp. 305-311.
- [5] Maljaars, J., and Soetens, F., "Strength of aluminium welds when exposed to fire," Proc. Sixth International Conference on Steel and Aluminium Structures, pp. 97-106.
- [6] 1998, Metals Handbook Desk Edition, ASM International, Materials Park, OH.
- [7] Mrowka-Nowotnik, G., and Sieniawski, J., 2005, "Influence of heat treatment on the microstructure and mechanical properties of 6005 and 6082 aluminum alloys," Journal of Materials Processing Technology, 162(163), pp. 367-372.
- [8] Hartawan, A., Thoe, T. B., Ng, S. T., Wu, H., and Liu, K., 2009, "Initial Investigation of Friction Stir Welding," SIMTech Technical Reports, 10(1).
- [9] Lakshminarayanan, A. K., Balasubramanian, V., and Elangovan, K., 2007, "Effect of welding processes on tensile properties of AA6061 aluminium alloy joints," The International Journal of Advanced Manufacturing Technology, 40(3-4), pp. 286-296.
- [10] Paik, J. K., and Duran, A., 2004, "Ultimate Strength of Aluminum Plates and Stiffened Panels for Marine Applications," Marine Technology, 41(3), pp. 108-121.
- [11] Mazzolani, F., 1995, Aluminium Alloy Structures, E & FN Spon, London, UK.
- [12] Erman Tekkaya, A., 2001, "Improved relationship between Vickers hardness and yield strength for cold formed materials," Steel Research, 72(8), pp. 304-310.
- [13] Maljaars, J., and Soetens, F., 2005, "Fire exposed aluminium structures," HERON, 50(4), pp. 261-278.
- [14] Amdahl, J., Langhelle, N., and Lundberg, S., 2001, "Aluminum Plated Structures at Elevated Temperatures," 20th Offshore Mechanics and Arctic Engineering Conference, ASME, Rio De Janeiro, Brazil, pp. 309-316.

- [15] Faggiano, B., De Matteis, G., Landolfo, R., and Mazzolani, F., 2004, "Behaviour of Aluminum Alloy Structures Under Fire," *Journal of Civil Engineering and Management*, 10(3), pp. 183-190.
- [16] Knobloch, M., and Fontana, M., 2005, "Load-carrying Behavior of Unstiffened Elements at Elevated Temperatures in Fire," *Fire Safety Science*, 8, pp. 223-234.
- [17] Walker, S., and Tahan, N., 1993, "The Fire Resistance of Aluminium," *FABIG Newsletter*, 8, pp. 223-234.
- [18] Maljaars, J., Soetens, F., and Katgerman, L., 2008, "Constitutive Model for Aluminum Alloys Exposed to Fire Conditions," *Metallurgical and Materials Transactions A*, 39(4), pp. 778-789.
- [19] Kodur, V. K. R., and Dwaikat, M. M. S., 2010, "Effect of high temperature creep on the fire response of restrained steel beams," *Materials and Structures*, 43(10), pp. 1327-1341.
- [20] Dowling, N. E., 2007, *Mechanical Behavior of Materials*, Pearson Prentice Hall, Upper Saddle River, NJ.
- [21] Frost, H. J., 1982, *Deformation-Mechanism Maps The Plasticity and Creep of Metals and Ceramics*, Pergamon Press Inc., Elmsford, NY.
- [22] Boresi, A. P., and Schmidt, R. J., 2003, *Advanced Mechanics of Materials*, John Wiley & Sons, Inc.
- [23] Feih, S., Kandare, E., and Mouritz, A. P., 2010, "Aluminum Creep Data and Modelling Approaches."
- [24] "Abaqus 6.10 Online Documentation," Dassault Systemes.
- [25] Langhelle, N., Eberg, E., Amdahl, J., and Lundberg, S., "Buckling Tests of Aluminium Columns at Elevated Temperatures," *Proc. International Conference on Offshore Mechanics and Arctic Engineering (OMAЕ)*, pp. 387-394.
- [26] Maljaars, J., Soetens, F., and Snijder, H. H., 2009, "Local buckling of aluminium structures exposed to fire Part 1: Tests," *Thin-Walled Structures*, 47(11), pp. 1404-1417.
- [27] Maljaars, J., Soetens, F., and Snijder, H. H., 2009, "Local buckling of aluminium structures exposed to fire Part 2: Finite element models," *Thin-Walled Structures*, 47(11), pp. 1418-1428.
- [28] Roper, J. R., 2005, "Finite Element Modeling of Complex Welded Structures," *Welding Journal*, 84(12), pp. 42-45.
- [29] Dobmeier, J. M., Barton, F. W., Gomez, J. P., Massarelli, P. J., and McKeel, W. T., 1999, "Analytical and Experimental Evaluation of an Aluminum Bridge Deck Panel Part I:

- Service Load Performance," Virginia Transportation Research Council (VTRC), Charlottesville, VA.
- [30] Dobmeier, J. M., Barton, F. W., Gomez, J. P., Massarelli, P. J., and McKeel, W. T., 1999, "Analytical and Experimental Evaluation of an Aluminum Bridge Deck Panel Part II: Failure Analysis," Virginia Transportation Research Council (VTRC), Charlottesville, VA.
- [31] Vaughan, R. E., and Schonberg, W. P., 1995, "An Inelastic Analysis of a Welded Aluminum Joint," *Metallurgical and Materials Transactions*, 26(B), pp. 1253-1261.
- [32] Fogle, E. J., 2010, "Compression Failure of Aluminum Plates Exposed to Constant Heat Flux," Master of Science, Virginia Polytechnic Institute and State University, Blacksburg.
- [33] Sun, E. Q., "Shear Locking and Hourglassing in MSC Nastran, ABAQUS, and ANSYS," Proc. VPD Conference, Avar, Inc.
- [34] Feih, S., Arthur, K., and Case, S., 2011, "Shell element formulation in Abaqus."
- [35] Kandare, E., Feih, S., Kootsookos, A., Mathys, Z., Lattimer, B., and Mouritz, A. P., 2010, "Creep-Based Life Prediction Modeling of Aluminum in Fire," *Materials Science and Engineering*, A(527), pp. 1185-1193.
- [36] Feih, S., 2010, "Modeling of buckling characteristics of aluminum intermediate scale tests with imperfections," Virginia Tech, Blacksburg, VA.